Group resonant interactions between surface and internal gravity waves in a two-layer system

Tore Magnus A. Taklo[1] and Wooyoung Choi[1],†

[1]Department of Mathematical Sciences, New Jersey Institute of Technology, Newark, NJ 07102-1982, USA

Nonlinear interactions between surface and internal gravity waves in a two-layer system are studied using explicit second-order nonlinear evolution equations in Hamiltonian form. Motivated by the detailed experiment of Lewis, Lake & Ko (*J. Fluid Mech.*, vol. 63, 1974, pp. 773–800), our focus is on surface wave modulation by the group resonance mechanism that corresponds to near-resonant triad interactions between a long internal wave and short surface waves. Our numerical solutions show good agreement with laboratory measurements of the local wave amplitude and slope, and confirm that the surface modulation becomes significant when the group velocity of the surface waves matches the phase speed of the internal wave, as the linear modulation theory predicts. It is shown, however, that, after the envelope amplitude is increased sufficiently, the surface and internal waves start to exchange energy through near-resonant triad interactions, which is found to be crucial to accurately describe the long-term surface wave modulation by an internal wave. The reduced amplitude equations are also adopted to validate this observation. For oceanic applications, numerical solutions are presented for a density ratio close to one and it is found that significant energy exchanges occur through primary and successive resonant triad interactions.

---

1. Introduction

Internal waves occur between subsurface layers in water that is stratified due to temperature and salinity variations. Observations from remote sensing, as well as *in situ* measurements, have demonstrated that internal waves can substantially change the top free surface of the ocean (Hughes & Grant 1978; Osborne & Burch 1980; Alpers 1985; Gasparovic, Apel & Kasischke 1988; Watson & Robinson 1990). Basic signatures reported are surface roughness and slicks that are characterized by areas of increased surface wave steepness and wide bands of smooth water surface, respectively. Such surface signatures have been also observed in laboratory experiments in a two-layer system, for example, by Lewis, Lake & Ko (1974) for a monochromatic internal wave train and by Kodaira *et al.* (2016) for an internal

† Email address for correspondence: wychoi@njit.edu

solitary wave. The observed surface signatures were then attributed to short surface waves modulated by the long internal wave through near-resonant triad interactions.

For surface gravity waves on a homogeneous fluid, resonant interactions are possible among four waves at third-order nonlinearity (Phillips 1960) although three-wave resonant interactions can occur among gravity–capillary waves (McGoldrick 1965). On the other hand, in a two-layer density-stratified fluid, it is well known that three-wave resonant interactions are possible between surface and internal gravity waves at second-order nonlinearity, even in the absence of surface tension.

The exact resonance conditions for one-dimensional surface and internal gravity waves have been identified, for convenience, as three different classes. While the class-I (Ball 1964) and class-II (Segur 1980; Wen 1995; Hill & Foda 1996) resonance conditions are for counter-propagating waves, the class-III (Alam 2012) resonance conditions are for co-propagating waves. Recently, much attention has been paid to the class-III resonance that occurs among two short surface waves and one, relatively longer, internal wave. Alam (2012) studied the class-III resonance in detail with a third-order high-order spectral (HOS) method and observed a cascade of surface wave energy through successive resonant triad interactions. More general interactions between broadband surface and internal waves were studied numerically using a second-order HOS method by Tanaka & Wakayama (2015).

In this paper, we focus on the modulation of short surface waves satisfying the so-called group resonance condition, which is an approximation to the class-III resonance condition and requires the group velocity of the surface waves to match the phase speed of a long internal wave. As the group resonance condition can be easily met under realistic oceanic conditions, this phenomenon has been investigated for several decades both theoretically and experimentally with special emphasis on the critical case relevant for internal solitary waves (as discussed in § 2.1). For example, after imposing the group resonance condition, Funakoshi & Oikawa (1983) derived a reduced weakly nonlinear model for the mutual interaction between short surface and long internal waves. This is a generalization of the model of Kawahara, Sugimoto & Kakutani (1975) and Benney (1977), who studied the interaction between long and short surface gravity–capillary waves on a homogeneous layer. However, the reduced model obtained by Funakoshi & Oikawa (1983) is incomplete in describing the surface current variation induced by the long internal wave, which is crucial in explaining surface wave modulation. In addition, Jiang *et al.* (2019) studied a similar wave interaction in a two-fluid system, but, as they used a weakly nonlinear long wave model for both surface and internal waves, the dispersion relation for short surface waves and, therefore, resonance conditions are not accurately modelled. Recently, among others, Hwung, Yang & Shugan (2009) and Craig, Guyenne & Sulem (2012) studied surface signatures of internal solitary waves using reduced models for surface and internal wave interactions.

Motivated by the previous observations of Ewing (1950), LaFond (1962) and Gargett & Hughes (1972), the group resonance was investigated experimentally by Lewis *et al.* (1974) by generating simultaneously a short surface wave with a small amplitude and a long internal wave with a relatively large amplitude in a wave tank. Using the fact that the internal wave in the experiment remained almost unchanged, Lewis *et al.* (1974) modelled the internal wave effect as a surface current and described the observed surface wave modulation as the surface wave–current interaction using the linear modulation theory (Longuet-Higgins & Stewart 1960, 1961; Whitham 1962; Gargett & Hughes 1972; Phillips 1977; Hughes 1978). Significant modulation of the free surface was observed in the experiment and was quantified in

terms of local amplitude and slope variations. It was found that the most significant modulation occurs when the group velocity of the surface waves is close to the phase speed of the internal wave, which is consistent with the group resonance condition. Therefore, it is confirmed that the group resonance mechanism plays a major role in describing modulated short surface waves that interact with long internal waves. Despite its success in comparison with experimental observations, the linear modulation theory that Lewis *et al.* (1974) used with a prescribed current field is unable to describe any energy exchange between surface and internal waves, which could be important for surface modulation over a longer time scale.

Here, we develop an explicit Hamiltonian system correct to the second order in wave steepness using a weakly nonlinear asymptotic expansion approach adopted by Choi (1995). Then, under the group resonance condition, we solve the system numerically and compare in detail the numerical solutions with the experiments of Lewis *et al.* (1974) along with the linear modulation theory. In particular, we investigate the long-term evolution of modulated surface waves, for which no measurements were made in Lewis *et al.* (1974).

The paper is organized as follows. After discussing in § 2 the class-III resonance condition, an explicit second-order Hamiltonian system is obtained using an asymptotic expansion technique in § 3. The numerical model to solve the system is described in § 4 and is validated with the Stokes wave solutions of Thorpe (1968) and the numerical solutions of Alam (2012) for exact resonant interactions using the HOS method. In § 5, the experiment of Lewis *et al.* (1974) and the linear modulation theory are revisited and analytic expressions for surface wave amplitude and slope variations are obtained. In § 6, the numerical solutions of the Hamiltonian system are compared with the measurements of Lewis *et al.* (1974). In § 7, the results are discussed with the amplitude equations of the primary resonant triad and numerical solutions for a more realistic density ratio are presented. Finally concluding remarks are given in § 8.

2. Near-resonant class-III interactions

For a system of two layers of densities ρ_i and thicknesses h_i with $i = 1$ and 2 corresponding to the upper and lower layers, respectively, the linear dispersion relation can be obtained (Lamb 1932) by solving

$$(\rho_1 T_1 T_2 + \rho_2)\omega^4 - \rho_2 gk(T_1 + T_2)\omega^2 + (\rho_2 - \rho_1)g^2 k^2 T_1 T_2 = 0, \qquad (2.1)$$

where g is the gravitational acceleration, ω is the wave frequency, k is the wavenumber and $T_i = \tanh(kh_i)$. Equation (2.1) has two positive real roots for ω^2, say ω_+^2 and ω_-^2, which correspond to the frequencies of fast surface (or barotropic) and slow internal (or baroclinic) wave modes.

For the class-III resonant triad interactions, we consider two short surface waves and one long internal wave propagating in the same direction. After introducing K and Ω for the wavenumber and frequency of the internal wave to distinguish them from those of the surface wave (denoted hereafter by k and ω), the resonance conditions are given by

$$k_1 - k_2 \pm K = 0, \qquad (2.2a)$$
$$\omega_1 - \omega_2 \pm \Omega = 0, \qquad (2.2b)$$

where $\omega_j = \omega(k_j)$, and $k_{1_\pm}$, $k_{2_\pm}$, K and their corresponding wave frequencies are assumed positive. For one-dimensional waves, equation (2.2) has a one-parameter
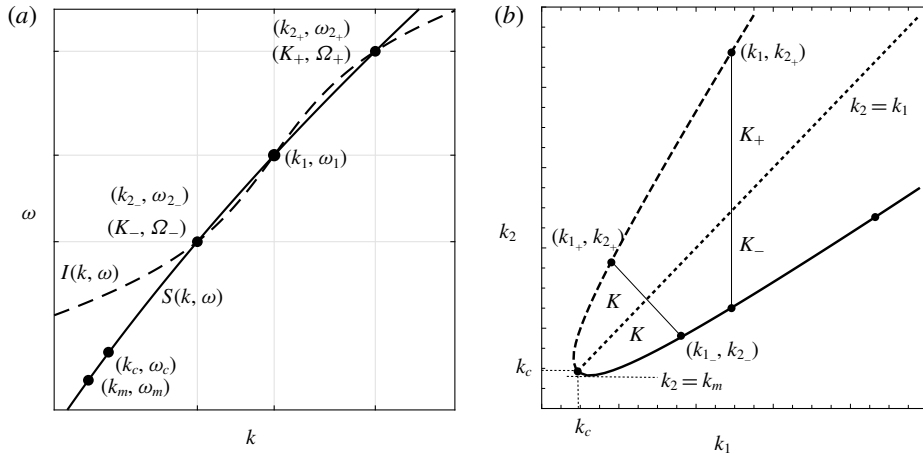
FIGURE 1. (a) Dispersion curves for surface (solid, denoted by S) and internal (dashed, I) waves. The two intersection points represent the class-III resonant triads for fixed k_1: $(k_1, k_{2_\pm}, K_\pm)$. Here, k_c represents the critical wavenumber defined by (2.3). For any surface wave whose wavenumber is greater than k_c, one can find two class-III resonant triads. On the other hand, k_m is the smallest possible wavenumber in a resonant triad. (b) Solution curves for the resonance condition given by (2.2). The solutions can be found for a fixed value of K or k_1.

family of solutions (two equations for three unknowns). For example, for a fixed value of k_1, one can find two sets of solutions: (k_1, k_{2_+}, K_+) and (k_1, k_{2_-}, K_-), as shown in figure 1(*a*).

Alternatively, for a fixed value of K, the solutions can be denoted by $(k_{1_\pm}, k_{2_\pm}, K)$ with $0 < K \ll k_{2_-} \leqslant k_{1_-}$ and $0 < K \ll k_{1_+} \leqslant k_{2_+}$. Similar inequalities hold for the corresponding wave frequencies $(\omega_{1_\pm}, \omega_{2_\pm}, \Omega)$. As there is no real distinction between the surface waves of k_1 and k_2 that share the same dispersion relation, one can find the solution on one branch from that on the other branch by interchanging the subscripts 1 and 2. For example, if (k_{1_-}, k_{2_-}, K) is the solution of (2.2) with the negative sign (the negative branch), $(k_{1_+}, k_{2_+}, K) = (k_{2_-}, k_{1_-}, K)$ is the solution set on the positive branch, as shown in figure 1(*b*).

2.1. *Critical wavenumber*

It is known that the class-III resonance occurs only when the slope of the dispersion curve for the surface wave at (k_1, ω_1) is smaller than that for the internal wave at $(K, \Omega) = (0, 0)$ (see figure 1*a*). This can happen only when k_1 is greater than a certain critical value k_c. Considering that the two dispersion curves should be tangent to each other as $k_1(= k_2) \to k_c$ and $K \to 0$, the critical surface wavenumber can be found by matching the slopes of the two curves: $\mathrm{d}\Omega/\mathrm{d}K|_{K=0} = \mathrm{d}\omega/\mathrm{d}k|_{k=k_c}$. From $\mathrm{d}\Omega/\mathrm{d}K|_{K=0} = \Omega/K|_{K=0}$, the criticality condition implies that the linear long wave speed of the internal wave $C_0 = \Omega/K|_{K=0}$ and the group velocity of the surface wave $c_g(k_c) = \mathrm{d}\omega/\mathrm{d}k|_{k=k_c}$ must be equal to each other so that
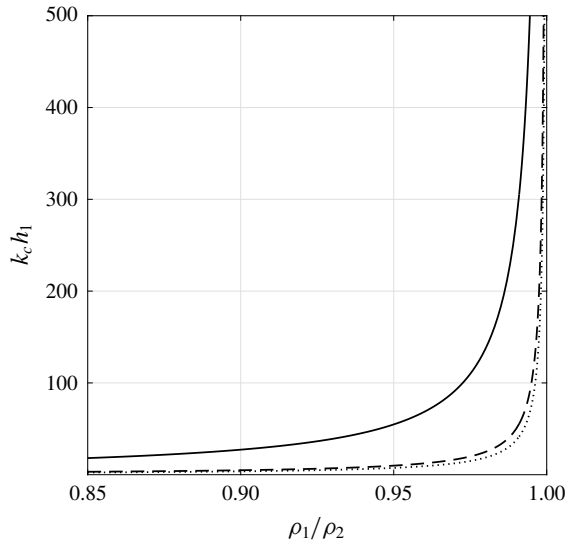
$$C_0 = c_g(k_c), \tag{2.3}$$

FIGURE 2. The critical wavenumber $k_c h_1$ as a function of the density ratio for ρ_1/ρ_2 between 0.85 and 1 for three different depth ratios: $h_1/h_2 = 10$ (solid); $h_1/h_2 = 1$ (dashed); $h_1/h_2 = 1/2$ (dotted).

where C_0 is the linear long internal wave speed given by

$$C_0{}^2 = \frac{gh_1 h_2(\rho_2 - \rho_1)}{\rho_1 h_2 + \rho_2 h_1}. \tag{2.4}$$

Then, it can be concluded from (2.3) that the class-III resonance is always possible when at least one of the surface wavenumbers is greater than k_c, which depends on the density and depth ratios: $k_c = k_c(\rho_1/\rho_2, h_1/h_2)$.

Figure 2 shows the dimensionless critical wavenumber $k_c h_1$ as a function of density ratio ρ_1/ρ_2 for values of the latter between 0.85 and 1 for different depth ratios h_1/h_2. The critical wavenumber $k_c h_1$ increases with ρ_1/ρ_2 and h_1/h_2. As the density ratio $\rho_1/\rho_2 \to 1$, the dimensionless critical wavenumber $k_c h_1$ increases rapidly and, therefore, only short surface waves satisfy the class-III resonance conditions given by (2.2). For example, for $\rho_1/\rho_2 = 0.99$ and $h_1/h_2 = 1/2$, one can find $k_c h_1 \simeq 37.42$ so that the critical wavelength $\lambda_c = 2\pi/k_c$ is given by $\lambda_c/h_1 \simeq 0.168$.

2.2. *Group resonance condition near criticality*

Near criticality, the two surface wavenumbers k_1 and k_2 are close to each other so that k_2 can be written as $k_2 = k_1(1 \pm K/k_1)$ with $K/k_1 \ll 1$. When $\omega_2 = \omega(k_2)$ is expanded around k_1, one can show that

$$\omega_1 - \omega_2 \pm \Omega = \mp \left.\frac{d\omega}{dk}\right|_{k_1} K \pm \Omega + O(K/k_1)^2. \tag{2.5}$$

This implies that the resonance condition given by (2.2*b*) can be satisfied approximately under the so-called group resonance condition defined by

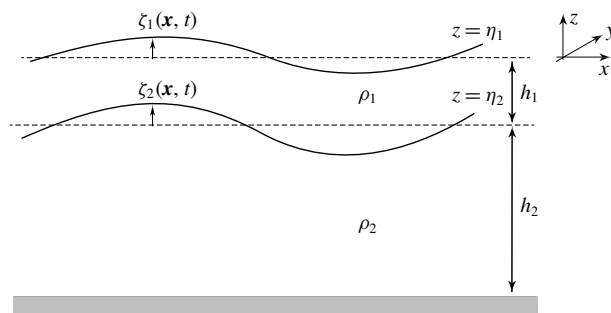$$C|_K \simeq c_g|_{k_g}, \tag{2.6}$$

FIGURE 3. Two-layer system.

where k_g is the wavenumber of the carrier wave whose group velocity matches the phase speed of the internal wave $C = \Omega/K$. This condition is a slight modification to (2.3) for an internal wave whose wavenumber is small, but not zero.

Since (2.6) is an approximation to (2.2b), its solution k_g is slightly different from $k_{1\pm}$, which are the solutions of the exact resonance condition (2.2) for a fixed value of K. Therefore, the triads of $(k_g, k_g \pm K, K)$ satisfy a near-resonance condition.

In this paper, we develop an explicit Hamiltonian system and study the near-resonant triad interactions between short surface and long internal waves under the group resonance condition. Then the results will be compared with previous theoretical and experimental results.

3. Explicit Hamiltonian system for two-layer flows

3.1. *Basic equations*

We consider a system of two layers with constant densities, where the ith layer $(i = 1, 2)$ is bounded by the upper and lower boundaries located at $z = \eta_i(\boldsymbol{x}, t)$ and $z = \eta_{i+1}(\boldsymbol{x}, t)$, respectively, with $\boldsymbol{x} = (x, y)$. Here, $\eta_1 = \zeta_1$, $\eta_2 = -h_1 + \zeta_2$, $\eta_3 = -(h_1 + h_2)$ with $\zeta_1(\boldsymbol{x}, t)$ and $\zeta_2(\boldsymbol{x}, t)$ being the surface and interface displacements, respectively (see figure 3).

Under the potential flow assumption, the kinematic boundary condition at the upper boundary of the ith layer is given, after using the chain rule, by

$$\frac{\partial \zeta_i}{\partial t} + \nabla \Phi_i \cdot \nabla \zeta_i = \left(1 + |\nabla \zeta_i|^2\right) W_i, \tag{3.1}$$

where ∇ is the horizontal gradient, and $i = 1$ and 2 correspond to the upper and lower layers, respectively. Here, Φ_i and W_i are the velocity potential and the vertical velocity, respectively, evaluated at $z = \eta_i$ such that $\Phi_i(\boldsymbol{x}, t) \equiv \phi_i(\boldsymbol{x}, z = \eta_i, t)$ and $W_i(\boldsymbol{x}, t) \equiv \partial \phi_i/\partial z(\boldsymbol{x}, z = \eta_i, t)$, with ϕ_i being the solution of the three-dimensional Laplace equation for the ith layer. In addition, the kinematic boundary condition at the interface $(z = \eta_2)$ can be written, in terms of the velocity potential for the upper layer, as

$$\frac{\partial \zeta_2}{\partial t} + \nabla \Phi_1^* \cdot \nabla \zeta_2 = \left(1 + |\nabla \zeta_2|^2\right) W_1^*. \tag{3.2}$$

Here, the variables with asterisks represent those evaluated at the interface such that $\Phi_1^* \equiv \phi_1|_{z=\eta_2}$ and $W_1^* \equiv \partial \phi_1/\partial z|_{z=\eta_2}$. When combined with (3.1), the second kinematic

condition given by (3.2) can be written as

$$W_1^* - \frac{\nabla \zeta_2}{1 + |\nabla \zeta_2|^2} \cdot \nabla \Phi_1^* = W_2 - \frac{\nabla \zeta_2}{1 + |\nabla \zeta_2|^2} \cdot \nabla \Phi_2, \tag{3.3}$$

which implies continuity of the normal velocities at the interface located at $z = \eta_2$, or $z = -h_2 + \zeta_2(x, t)$.

On the other hand, the dynamic boundary conditions at the top free surface and interface are given by

$$P_1 = P_{atm} \quad \text{at } z = \eta_1, \quad P_2 = P_1^* \quad \text{at } z = \eta_2, \tag{3.4a,b}$$

where P_i ($i = 1, 2$) are the pressures evaluated at $z = \eta_i$ while P_1^* is the pressure of the upper layer evaluated at the interface ($z = \eta_2$). Here, P_{atm} is the applied atmospheric pressure in the presence of wind; otherwise, $P_{atm} = 0$. From the Bernoulli equation given, after being evaluated at $z = \eta_i$, by

$$\frac{\partial \Phi_i}{\partial t} + g\eta_i + \frac{1}{2}|\nabla \Phi_i|^2 + \frac{P_i}{\rho_i} = \frac{1}{2}(1 + |\nabla \zeta_i|^2)W_i^2, \tag{3.5}$$

the dynamic boundary conditions (3.4) can be written as

$$\frac{\partial \Psi_1}{\partial t} = -\rho_1 g \zeta_1 - \frac{1}{2}\rho_1 |\nabla \Phi_1|^2 + \frac{1}{2}\rho_1(1 + |\nabla \zeta_1|^2)W_1^2 - P_{atm}, \tag{3.6}$$

$$\frac{\partial \Psi_2}{\partial t} = -\Delta \rho g \zeta_2 - \frac{1}{2}(\rho_2|\nabla \Phi_2|^2 - \rho_1|\nabla \Phi_1^*|^2) + \frac{1}{2}(1 + |\nabla \zeta_2|^2)(\rho_2 W_2^2 - \rho_1 W_1^{*2}), \tag{3.7}$$

where $\Delta \rho = \rho_2 - \rho_1 > 0$ for stable stratification and Ψ_i are defined as

$$\Psi_1 = \rho_1 \Phi_1, \quad \Psi_2 = \rho_2 \Phi_2 - \rho_1 \Phi_1^*. \tag{3.8a,b}$$

Once Φ_i, W_i, Φ_1^* and W_1^* can be expressed in terms of ζ_i and Ψ_i, equations (3.1) and (3.6)–(3.7) yield a closed system of nonlinear evolution equations for ζ_i and Ψ_i ($i = 1, 2$).

As shown by Benjamin & Bridges (1997) for unbounded two-layer flows, the system for ζ_i and Ψ_i is of particular interest as it is known to have a Hamiltonian structure such that

$$\frac{\partial \zeta_i}{\partial t} = \frac{\delta E}{\delta \Psi_i}, \quad \frac{\partial \Psi_i}{\partial t} = -\frac{\delta E}{\delta \zeta_i}, \tag{3.9a,b}$$

where $E = E_p + E_K$ is the total energy with the potential energy E_p and the kinetic energy E_K given by

$$E_P = \frac{1}{2} \int \left[\rho_1 g \zeta_1^2 + (\rho_2 - \rho_1)g\zeta_1^2 \right] \, \mathrm{d}x, \tag{3.10}$$

$$E_K = \frac{1}{2} \int \left(\sum_{i=1}^{2} \Psi_i \frac{\partial \zeta_i}{\partial t} \right) \, \mathrm{d}x. \tag{3.11}$$

For weakly nonlinear waves with $\epsilon \ll 1$ being the typical wave steepness, the nonlinear evolution equations given by (3.1) and (3.6)–(3.7) can be truncated at $O(\epsilon^2)$ as

$$\frac{\partial \zeta_1}{\partial t} = W_1 - \nabla \Phi_1 \cdot \nabla \zeta_1 + O(\epsilon^3), \quad \frac{\partial \zeta_2}{\partial t} = W_2 - \nabla \Phi_2 \cdot \nabla \zeta_2 + O(\epsilon^3), \tag{3.12a,b}$$

$$\frac{\partial \Psi_1}{\partial t} = -\rho_1 g \zeta_1 - \frac{1}{2} |\nabla \Psi_1|^2/\rho_1 + \frac{1}{2} \rho_1 W_1^{\,2} + O(\epsilon^3), \tag{3.13}$$

$$\frac{\partial \Psi_2}{\partial t} = -\Delta \rho g \zeta_2 - \frac{1}{2} \left(\rho_2 |\nabla \Phi_2|^2 - \rho_1 |\nabla \Phi_1^*|^2 \right) + \frac{1}{2} \left(\rho_2 W_2^{\,2} - \rho_1 W_1^{*2} \right) + O(\epsilon^3), \tag{3.14}$$

where $W_i = O(|\nabla \zeta_i|) = O(|\nabla \Phi_i|) = O(|\nabla \Psi_i|) = O(\epsilon)$ have been assumed on the right-hand sides.

In the followings, using asymptotic expansion correct up to $O(\epsilon^2)$, we first find the explicit expressions for W_i $(i = 1, 2)$ correct to $O(\epsilon^2)$ and those for W_1^*, and Φ_1^* correct to $O(\epsilon)$ in terms of ζ_i and Φ_i. Then, by expressing Φ_i in terms of ζ_i and Ψ_i, we obtain a closed system for ζ_i and Ψ_i.

3.2. *Linear solutions*

The solution of the Laplace equation for the ith layer can be written as

$$\phi_i(\boldsymbol{k}, z, t) = A_i(\boldsymbol{k}, t) \cosh(kz) + B_i(\boldsymbol{k}, t) \sinh(kz). \tag{3.15}$$

To determine A_i and B_i, we impose the following linearized boundary conditions at $z = z_i$ and $z = z_{i+1}$ for $i = 1, 2$

$$\phi_i = \overline{\phi}_i \quad \text{at } z = z_i, \tag{3.16}$$

$$\frac{\partial \phi_i}{\partial z} = w_i^* \quad \text{at } z = z_{i+1}, \tag{3.17}$$

where $z = z_i$ and $z = z_{i+1}$ are the mean positions of the upper and lower boundaries, respectively, of the ith layer so that $z_1 = 0$, $z_2 = -h_1$ and $z_3 = -(h_1 + h_2)$. Here, we impose the Dirichlet and Neumann boundary conditions at the mean upper and lower boundaries, respectively, for convenience in the derivation of a model. For example, for the lower layer ($i = 2$), the zero Neumann condition ($w_2^* = 0$) needs to be imposed at $z = z_3$ as the vertical velocity vanishes at the bottom. After imposing the boundary conditions given by (3.16) and (3.17) on the solution of the Laplace equation given by (3.15), we attempt to find the expressions for $\overline{w}_i$ and ϕ_i^* in terms of $\overline{\phi}_i$ and w_i^*. Notice that $\overline{f}_i$ and f_i^* represent the variables evaluated at $z = z_i$ and $z = z_{i+1}$, respectively.

The linear solution for the ith layer satisfying the boundary conditions given by (3.16)–(3.17) can be found as

$$\phi_i = \frac{1}{k \cosh[k(z_i - z_{i+1})]} (k \cosh[k(z - z_{i+1})] \overline{\phi}_i + \sinh[k(z - z_i)] w_i^*). \tag{3.18}$$

Then, the expressions for $\overline{w}_i = \partial \phi_i/\partial z|_{z=z_i}$ and $\phi_i^* = \phi_i|_{z=z_{i+1}}$ can be obtained, in terms of $\overline{\phi}_i$ and w_i^*, as

$$\overline{w}_i = kT_i \overline{\phi}_i + S_i w_i^*, \quad \phi_i^* = S_i \overline{\phi}_i - (T_i/k) w_i^*, \tag{3.19a,b}$$

where $z_i - z_{i+1} = h_i$ has been used, and T_i and S_i are given by

$$T_i = \tanh kh_i, \quad S_i = \operatorname{sech} kh_i. \tag{3.20a,b}$$

Here, for example, the Fourier multiplier kT_i should be understood as $kT_i \overline{\phi}_i = L_T[\overline{\phi}_i]$, where L_T is a linear operator whose kernel is given by kT_i in Fourier space. For the lower layer ($i = 2$), as $w_2^* = 0$, the expressions of $\overline{w}_2$ and ϕ_2^* given by (3.19) are simplified to

$$\overline{w}_2 = kT_2 \overline{\phi}_2, \quad \phi_2^* = S_2 \overline{\phi}_2. \tag{3.21a,b}$$

3.3. *Second-order approximation*

To find the expressions for W_i correct to $O(\epsilon^2)$, we first expand both Φ_i and W_i about $z = z_i$ as

$$\Phi_i = \overline{\phi}_i + \zeta_i \overline{w}_i + O(\epsilon^3) = \overline{\phi}_i + \zeta_i \left(kT_i \overline{\phi}_i + S_i w_i^* \right) + O(\epsilon^3), \tag{3.22}$$

$$W_i = \overline{w}_i - \zeta_i \nabla^2 \overline{\phi}_i + O(\epsilon^3) = kT_i \overline{\phi}_i + S_i w_i^* - \zeta_i \nabla^2 \overline{\phi}_i + O(\epsilon^3), \tag{3.23}$$

where (3.19) and $\partial^2 \phi_i / \partial z^2 |_{z=z_i} = -\nabla^2 \overline{\phi}_i$ have been used. After solving (3.22) iteratively to find the following expression for $\overline{\phi}_i$ in terms of Φ_i and w_i^*

$$\overline{\phi}_i = \Phi_i - \zeta_i (kT_i \overline{\phi}_i + S_i w_i^*) + O(\epsilon^3) = \Phi_i - \zeta_i (kT_i \Phi_i + S_i w_i^*) + O(\epsilon^3), \tag{3.24}$$

W_i can be expressed, from (3.23), as

$$W_i = kT_i \Phi_i + S_i w_i^* - \zeta_i \nabla^2 \Phi_i - kT_i [\zeta_i (kT_i \Phi_i + S_i w_i^*)] + O(\epsilon^3). \tag{3.25}$$

Similarly to (3.22)–(3.23), Φ_1^* and W_1^* can be expanded about $z = z_2$ as

$$\Phi_1^* = \phi_1^* + \zeta_2 w_1^* + O(\epsilon^3), \tag{3.26}$$

$$W_1^* = w_1^* - \zeta_2 \nabla^2 \phi_1^* + O(\epsilon^3), \tag{3.27}$$

which can be re-written, using (3.19) and (3.24), as

$$\Phi_1^* = S_1 \Phi_1 - \frac{T_1}{k} w_1^* + \zeta_2 w_1^* - S_1 [\zeta_1 (kT_1 \Phi_1 + S_1 w_1^*)] + O(\epsilon^3), \tag{3.28}$$

$$W_1^* = w_1^* - \zeta_2 \nabla^2 (S_1 \Phi_1 - \frac{T_1}{k} w_1^*) + O(\epsilon^3). \tag{3.29}$$

While $w_2^* = 0$, one still needs to find the expressions for w_1^* in terms of Φ_i and ζ_i, which can be obtained from the kinematic interface boundary condition (3.3) approximated to $O(\epsilon^2)$ by

$$W_1^* = W_2 - \nabla \zeta_2 \cdot \nabla \Phi_2 + \nabla \zeta_2 \cdot \nabla \Phi_1^* + O(\epsilon^3). \tag{3.30}$$

By substituting (3.25), (3.28) and (3.29) into (3.30), one can find iteratively the expression for w_1^* in terms of Φ_i and ζ_i as

$$w_1^* = kT_2 \Phi_2 - \nabla \cdot (\zeta_2 \nabla \Phi_2) - kT_2 (\zeta_2 kT_2 \Phi_2)$$
$$+ \nabla \cdot [\zeta_2 \nabla (S_1 \Phi_1 - T_1 T_2 \Phi_2)] + O(\epsilon^3). \tag{3.31}$$

After substituting (3.31) into (3.25), the expressions for W_i can be found, in terms of ζ_i and Φ_i, as

$$W_1 = kT_1 \Phi_1 + SkT_2 \Phi_2 - \zeta_1 \nabla^2 \Phi_1 - kT_1 [\zeta_1 (kT_1 \Phi_1 + SkT_2 \Phi_2)]$$
$$+ S[-\nabla \cdot (\zeta_2 \nabla \Phi_2) - kT_2 (\zeta_2 kT_2 \Phi_2) + \nabla \cdot \{\zeta_2 \nabla (S\Phi_1 - T_1 T_2 \Phi_2)\}] + O(\epsilon^3), \tag{3.32}$$

$$W_2 = kT_2 \Phi_2 - \zeta_2 \nabla^2 \Phi_2 - kT_2 (\zeta_2 kT_2 \Phi_2) + O(\epsilon^3), \tag{3.33}$$

where $S = S_1$. Then, from (3.28)–(3.29), the expressions for Φ_1^* and W_1^* correct to $O(\epsilon)$ can be found, in terms of ζ_i and Φ_i, as

$$\Phi_1^* = S\Phi_1 - \frac{T_1}{k} (kT_2 \Phi_2) + O(\epsilon^2), \quad W_1^* = kT_1 \Phi_1 + O(\epsilon^2). \tag{3.34a,b}$$

To obtain an explicit Hamiltonian system, there remains one more step to write Φ_2 in terms of the conjugate variables: ζ_i and Ψ_i. By substituting (3.31) into (3.28) and using $\Phi_1^* = (\rho_2 \Phi_2 - \Psi_2)/\rho_1$ from the definition of Ψ_2, one can find the expression for Ψ_2 as

$$\Psi_2 = (\rho_1 T_1 T_2 + \rho_2)\Phi_2 - \rho_1 S\Phi_1 - \rho_1[-S(\zeta_1(kT_1\Phi_1 + SkT_2\Phi_2)) + \zeta_2 kT_2\Phi_2]$$
$$-\rho_1 \frac{T_1}{k}[kT_2(\zeta_2 kT_2\Phi_2) + \nabla \cdot (\zeta_2 \nabla \Phi_2) - \nabla \cdot \{\zeta_2 \nabla(S\Phi_1 - T_1 T_2 \Phi_2)\}] + O(\epsilon^3), \quad (3.35)$$

which can be inverted iteratively to find the following expression for Φ_2 correct up to $O(\epsilon^2)$

$$\Phi_2 = J\left[(\Psi_2 + S\Psi_1) - S\zeta_1 kT_1\Psi_1 - \rho_1(S\zeta_1 S - \zeta_2)kT_2 J(\Psi_2 + S\Psi_1)\right.$$
$$\left. -\frac{T_1}{k}\nabla \cdot (\zeta_2 \nabla S\Psi_1) + \rho_1 \frac{T_1}{k}(kT_2\zeta_2 kT_2 + \nabla \cdot \zeta_2(1 + T_1 T_2)\nabla)J(\Psi_2 + S\Psi_1)\right], \quad (3.36)$$

where $\Psi_1 = \rho_1 \Phi_1$ has been used and J is defined as

$$J = 1/(\rho_1 T_1 T_2 + \rho_2). \quad (3.37)$$

3.4. *Second-order evolution equations*

By using (3.36) along with $\Phi_1 = \Psi_1/\rho_1$, one can express W_i, Φ_i^* and W_i^*, in terms of ζ_i and Ψ_i, from (3.32)–(3.34). Then, after substituting their expressions into (3.12)–(3.14), one can obtain a system of nonlinear evolution equations for ζ_i and Ψ_i ($i = 1, 2$) correct to $O(\epsilon^2)$, after lengthy manipulations, as

$$\frac{\partial \zeta_1}{\partial t} = \Gamma_{11}[\Psi_1] + \Gamma_{12}[\Psi_2] - \nabla \cdot (\zeta_1 \nabla \Psi_1)/\rho_1$$
$$- \rho_1 \Gamma_{11}\left[\zeta_1\left(\Gamma_{11}[\Psi_1] + \Gamma_{12}[\Psi_2]\right)\right] - \Delta\rho \Gamma_{21}\left[\zeta_2\left(\Gamma_{21}[\Psi_1] + \Gamma_{22}[\Psi_2]\right)\right]$$
$$+ \Delta\rho\,(\rho_2/\rho_1)\Gamma_{31}\left[\nabla \cdot (\zeta_2 \nabla \Gamma_{31}[\Psi_1])\right] - \rho_2 \Gamma_{31}\left[\nabla \cdot (\zeta_2 \nabla \Gamma_{33}[\Psi_2])\right], \quad (3.38a)$$

$$\frac{\partial \zeta_2}{\partial t} = \Gamma_{21}[\Psi_1] + \Gamma_{22}[\Psi_2] - \rho_1 \Gamma_{12}\left[\zeta_1\left(\Gamma_{11}[\Psi_1] + \Gamma_{12}[\Psi_2]\right)\right]$$
$$- \Delta\rho \Gamma_{22}\left[\zeta_2\left(\Gamma_{21}[\Psi_1] + \Gamma_{22}[\Psi_2]\right)\right] - \rho_2\,\Gamma_{33}\left[\nabla \cdot (\zeta_2 \nabla \Gamma_{31}[\Psi_1])\right]$$
$$- \rho_2 \Gamma_{30}\left[\nabla \cdot (\zeta_2 \nabla \Gamma_{30}[\Psi_2])\right] + \rho_1 \Gamma_{32}\left[\nabla \cdot (\zeta_2 \nabla \Gamma_{32}[\Psi_2])\right], \quad (3.38b)$$

$$\frac{\partial \Psi_1}{\partial t} = -\rho_1 g\zeta_1 + \frac{1}{2}\rho_1\left(\Gamma_{11}[\Psi_1] + \Gamma_{12}[\Psi_2]\right)^2 - \frac{1}{2}(\nabla \Psi_1 \cdot \nabla \Psi_1)/\rho_1, \quad (3.38c)$$

$$\frac{\partial \Psi_2}{\partial t} = -\Delta\rho g\zeta_2 + \frac{1}{2}\Delta\rho\left(\Gamma_{21}[\Psi_1] + \Gamma_{22}[\Psi_2]\right)^2$$
$$+ \frac{1}{2}\Delta\rho(\rho_2/\rho_1)(\nabla \Gamma_{31}[\Psi_1]) \cdot (\nabla \Gamma_{31}[\Psi_1]) - \frac{1}{2}\rho_2(\nabla \Gamma_{30}[\Psi_2]) \cdot (\nabla \Gamma_{30}[\Psi_2])$$
$$+ \frac{1}{2}\rho_1(\nabla \Gamma_{32}[\Psi_2]) \cdot (\nabla \Gamma_{32}[\Psi_2]) - \rho_2(\nabla \Gamma_{31}[\Psi_1]) \cdot (\nabla \Gamma_{33}[\Psi_2]), \quad (3.38d)$$

where $\Delta\rho = \rho_2 - \rho_1$ and ∇ is the two-dimensional gradient. The linear integral operators Γ_{ij} can be evaluated, in Fourier space, as

$$\Gamma_{ij}[\cdot] = \mathcal{F}^{-1}[\gamma_{ij}\mathcal{F}[\cdot]], \quad (3.39)$$

where $\mathcal{F}$ and $\mathcal{F}^{-1}$ are the Fourier and inverse Fourier transforms, respectively, and the Fourier multipliers γ_{ij} are defined as

$$\left.\begin{array}{l} \gamma_{11} = kJ\big[(\rho_2/\rho_1)T_1 + T_2\big], \quad \gamma_{12} = \gamma_{21} = kJST_2, \quad \gamma_{22} = kJT_2, \\ \gamma_{30} = J, \quad \gamma_{31} = JS, \quad \gamma_{32} = JT_1T_2, \quad \gamma_{33} = J(1 + T_1T_2), \end{array}\right\} \tag{3.40}$$

with T_i $(i = 1, 2)$, $S = S_1$ and J defined in (3.20) and (3.37).

When the system given by (3.38) is linearized and $(\zeta_i, \Psi_i) \sim \exp[\mathrm{i}(kx - \omega t)]$ for $i = 1, 2$ are assumed, one can obtain the linear dispersion relation given by (2.1), as shown in appendix A. In addition, various limits of the system are also discussed in appendix A.

The nonlinear evolution equations for ζ_i and Ψ_i $(i = 1, 2)$ given by (3.38) are Hamilton's equations (3.9), where the Hamiltonian E is the total energy truncated at $O(\epsilon^3)$ given by

$$E = E_2 + E_3, \tag{3.41}$$

with

$$\begin{aligned} E_2 &= \frac{1}{2}\int \Big[\rho_1 g {\zeta_1}^2 + \Delta\rho g {\zeta_2}^2 \\ &\quad + \Psi_1\,(\Gamma_{11}[\Psi_1]) + \Psi_1\,(\Gamma_{12}[\Psi_2]) + \Psi_2\,(\Gamma_{21}[\Psi_1]) + \Psi_2\,(\Gamma_{22}[\Psi_2])\Big]\,\mathrm{d}x, \tag{3.42} \\ E_3 &= -\frac{1}{2}\int \Big[\zeta_1\big\{-\nabla\Psi_1 \cdot \nabla\Psi_1/\rho_1 + \rho_1\big(\Gamma_{11}[\Psi_1] + \Gamma_{12}[\Psi_2]\big)^2\big\} \\ &\quad + \zeta_2\big\{(\rho_2/\rho_1)\Delta\rho(\nabla\Gamma_{31}[\Psi_1]) \cdot (\nabla\Gamma_{31}[\Psi_1]) - 2\rho_2(\nabla\Gamma_{31}[\Psi_1]) \cdot (\nabla\Gamma_{33}[\Psi_2]) \\ &\quad + \rho_1(\nabla\Gamma_{32}[\Psi_2]) \cdot (\nabla\Gamma_{32}[\Psi_2]) - \rho_2(\nabla\Gamma_{30}[\Psi_2]) \cdot (\nabla\Gamma_{30}[\Psi_2]) \\ &\quad + \Delta\rho(\Gamma_{21}[\Psi_1] + \Gamma_{22}[\Psi_2])^2\big\}\Big]\,\mathrm{d}x. \tag{3.43} \end{aligned}$$

Therefore, the total energy given by (3.41) with (3.42)–(3.43) is conserved exactly.

Previously, the two-layer problem with a free surface was studied by Alam, Liu & Yue (2009) using the HOS method. While the truncated Euler equations for the same variables were solved in Alam *et al.* (2009), the right-hand sides of their system are not written so explicitly. Therefore, an extra numerical step is required to close their system and the total energy is conserved approximately. The explicit Hamiltonian system given by (3.38) is closed for four conjugate variables and is convenient for both numerical and theoretical studies. When it is written in spectral space, the explicit system provides a spectral model preserving the Hamiltonian structure (Choi, Chabane & Taklo 2020). While the Hamiltonian system is valid for waves propagating in two horizontal dimensions, only one-dimensional waves will be considered hereafter for the numerical studies.

4. Numerical method and validation

To solve numerically the system (3.38) in a computational domain of length *L*, we adopt for spatial discretization a pseudo-spectral method based on the fast Fourier transform algorithm with *M* Fourier modes. The linear integral operators Γ_{ij} are evaluated in Fourier space using (3.39). The smallest wavenumber resolved in Fourier space is given by $\Delta k = 2\pi/L$. Once the right-hand sides of (3.38) are evaluated, the system is integrated in time using a fourth-order Runge–Kutta scheme with time step Δt.

To avoid aliasing errors resulting from the use of truncated Fourier series, a low-pass filter is applied to eliminate one third of the highest wavenumber modes. The two-layer problem is known to be locally unstable and is in fact ill posed when the velocity jump ΔU across the interface is constant. While the jump induced by a periodic internal wave varies in space, the instability might be still present for some physical parameters, but the low-pass filter for de-aliasing is expected to remove unstable short waves. Therefore, the problem is expected to be regularized. Based on the local linear stability analysis for two-layer Euler equations by Jo & Choi (2008), small amplitude disturbances can grow by instability if their wavenumbers are greater than $2g(\rho_2 - \rho_1)/(\rho_1 \Delta U^2)$ when $kh_i \gg 1$ ($i = 1, 2$) and $(\rho_2 - \rho_1)/\rho_1 \ll 1$ are assumed. However, it should be remarked that, for the parameters in our simulations, the velocity jump is so small that the unstable wavenumbers are much greater than the critical wavenumber k_c or the highest wavenumber that we resolve.

During our computations, the total energy defined by (3.41) with (3.42)–(3.43) is monitored and the numerical accuracy is measured by the energy difference

$$\Delta E = E_0 - E_N, \tag{4.1}$$

where $E_0 = E(t = 0)$ and $E_N = E(t = t_N = N\Delta t)$ are the energies of the initial condition and the last time step N, respectively. Before we investigate numerically the evolution under the group resonance, we validate our numerical model by studying (i) the propagation of Stokes waves in a two-layer system with a free surface and (ii) exact resonant triad interactions between surface and internal waves.

4.1. *Stokes waves in a two-layer system with a free surface*

The numerical model is first tested with the second-order Stokes wave solutions for a two-layer system with a free surface obtained by Thorpe (1968), for which the surface and interface displacements ζ_i ($i = 1, 2$), respectively, are given by

$$\zeta_1 = \widetilde{a}_j^+ e^{i\theta} + \widetilde{a}_{2j}^+ e^{2i\theta} + C.C. + O(\epsilon^3) = \overline{a}^+[\cos\theta + \sigma_1(k_j\overline{a}^+)\cos(2\theta) + O(\epsilon^2)], \tag{4.2}$$

$$\zeta_2 = \widetilde{a}_j^- e^{i\theta} + \widetilde{a}_{2j}^- e^{2i\theta} + C.C. + O(\epsilon^3) = \overline{a}^-[\cos\theta + \sigma_2(k_j\overline{a}^-)\cos(2\theta) + O(\epsilon^2)], \tag{4.3}$$

where $\overline{a}^+ = 2\widetilde{a}_j^+$, $\overline{a}^- = 2\widetilde{a}_j^-$, $\theta = k_j x - \omega_j t$ and σ_i ($i = 1, 2$) are defined as

$$\sigma_1 = \widetilde{a}_{2j}^+/[2k_j(\widetilde{a}_j^+)^2], \quad \sigma_2 = \widetilde{a}_{2j}^-/[2k_j(\widetilde{a}_j^-)^2]. \tag{4.4a,b}$$

In Thorpe (1968) (Professor Thorpe has kindly provided these solutions after having corrected typos in his original paper), σ_i ($i = 1, 2$) are given explicitly by

$$\sigma_1 = \frac{(\Omega - T_1)^2}{\Omega}\cosh 2k_j h_1 \cosh^2 k_j h_1 \left[2\sigma_2\left(\overline{T}_1 + \frac{\rho_2}{\rho_1 \overline{T}_2} - \frac{\rho_2 - \rho_1}{2\rho_1 \Omega}\right)\right.$$
$$\left. - \frac{1}{4}\left\{2 + \frac{\rho_2(3 - T_2^2)}{\rho_1 T_2^2} + \frac{4(1 - \Omega T_1)\overline{T}_1}{\Omega - T_1} - \frac{(1 - \Omega^2)\cosh 2k_j h_1 - (1 - 3\Omega^2)}{(\Omega - T_1)^2 \cosh 2k_j h_1 \cosh^2 k_j h_1}\right\}\right], \tag{4.5}$$

$$\sigma_2 = \frac{\rho_1 \Omega \overline{T}_2}{4\mu}\left[(2\Omega - \overline{T}_1)\left\{2 + \frac{\rho_2(3 - T_2^2)}{\rho_1 T_2^2}\right\} + \frac{4(1 - \Omega T_1)(2\Omega\overline{T}_1 - 1)}{\Omega - T_1}\right.$$
$$\left. + (1 - \Omega^2)\frac{6\Omega - (2\Omega - \overline{T}_1)\cosh 2k_j h_1}{(\Omega - T_1)^2 \cosh 2k_j h_1 \cosh^2 k_j h_1}\right], \tag{4.6}$$
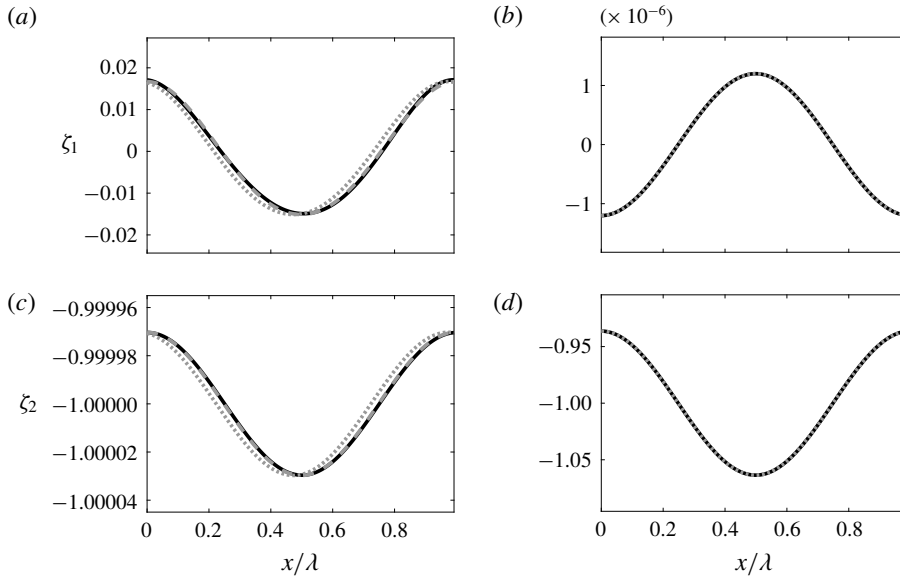
FIGURE 4. Numerical solutions for Stokes waves (solid line) compared with the second-order Stokes solution (dotted): (a,c) barotropic and (b,d) baroclinic modes after 10 wave periods. Notice that, for the barotropic mode, the comparison improves with the second-order Stokes solution with the nonlinear speed correction (dashed). The density and depth ratios are $\rho_1/\rho_2 = 0.99$ and $h_1/h_2 = 1/2$, respectively.

where $T_i = \tanh k_j h_i$, $\overline{T}_i = \tanh 2k_j h_i$,

$$\Omega = \omega_j^2/(gk_j), \quad \mu = 4\Omega^2(\rho_1\overline{T}_1\overline{T}_2 + \rho_2) - 2\rho_2\Omega(\overline{T}_1 + \overline{T}_2) + (\rho_2 - \rho_1)\overline{T}_1\overline{T}_2. \quad (4.7a,b)$$

Figure 4 shows the numerical solutions after 10 wave periods for the Stokes waves of the barotropic and baroclinic modes whose wave steepnesses (the product between the wave amplitude and the wavenumber) are $ka = 0.1$ and $KA = 0.4$, where a and A are the amplitudes of the surface and internal waves, respectively. Here, we use the number of Fourier modes $M = 2^7$ and the time step $\omega\Delta t = 0.01$ and $\Omega\Delta t = 0.007$ for the barotropic and baroclinic simulations, respectively. Then the total energy is conserved with $\Delta E/E_0 = 1.18 \times 10^{-8}$ and $\Delta E/E_0 = 1.6 \times 10^{-9}$ for the two simulations. The numerical solutions are in good agreement with the Stokes solutions, except for a slight difference in phase for the barotropic mode. While the second-order Stokes solutions of Thorpe (1968) have no corrections to the wave speeds, the Hamiltonian system yields a speed correction from the interaction between the first and second harmonics. When the Stokes wave solution of the barotropic mode is shifted with this speed correction, it agrees well with the corresponding numerical solution.

4.2. *Class-III resonant triads and comparison with a HOS model*

Alam (2012) studied a class-III resonant triad interaction using a third-order HOS method. An interesting feature observed in his study was that the initial energy of two waves can spread to several triads through successive resonant interactions. As in Alam (2012), we initialize the Hamiltonian system (3.38) with one surface and one
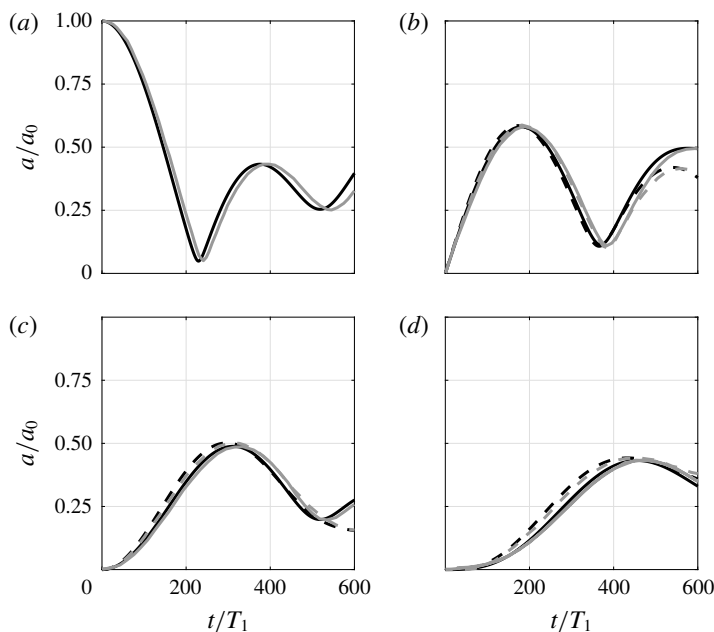
FIGURE 5. Evolution of surface wave amplitudes under resonant triad interactions: numerical solutions of the Hamiltonian system (3.38) (black curves) compared with those of Alam (2012) using the HOS method (grey curves). Solid curves: a_{n_-} ($n = 2, 3, 4$). Dashed curves: a_{n_+} ($n = 2, 3, 4$). (a) a_1. (b) $a_{2_\pm}$. (c) $a_{3_\pm}$. (d) $a_{4_\pm}$.

internal wave with wavenumbers $k_1 h_1 \simeq 8.014$ and $K h_1 \simeq 0.308$, respectively, in a two-layer system of $\rho_1/\rho_2 = 0.95$ and $h_1/h_2 = 1/2$. The corresponding wave steepnesses are $k_1 a_1 = 0.008$ and $KA = 0.001$, respectively. Considering the surface wavenumbers at resonance with the internal wave of $K h_1 \simeq 0.308$ are $k_1 h_1 \simeq 8.014$ and $k_{2_-} h_1 \simeq 7.706$, the interaction among the primary triad (k_1, k_{2_-}, K) can be considered the exact resonance.

In the computation, we choose the number of Fourier modes $M = 2^{11}$ and the time step $\omega_1 \Delta t = 0.1$, where ω_1 is the surface wave frequency. The total computation period is $600 T_1$, where T_1 is the surface wave period given by $T_1 = 2\pi/\omega_1$, and the total energy is conserved with $\Delta E/E_0 = 3.44 \times 10^{-4}$.

Figure 5 shows the time evolution of a_1 and $a_{n_\pm}$ ($n = 2, 3, 4$), where $a_{n_\pm}$ are the amplitudes of $k_{n_\pm} = k_1 \pm (n-1)K$. Notice that the amplitudes are normalized with the initial amplitude $a_0 = a_1(t = 0)$ of ζ_1. Through the resonant triad interaction of class III with two initial waves of K and k_1, the waves of $k_{2_\pm}$ are excited initially. As this primary triad interaction is exact, the three modes exchange their energies significantly so that the magnitudes of $a_{2_\pm}$ excited is comparable to that of a_1 and the variation of a_1/a_0 is $O(1)$. Although the wave steepnesses are rather small, the surface waves of $k_{n_\pm}$ ($n = 3, 4$) are also excited over longer time scales through successive near-resonant triad interactions (Alam 2012).

As can be observed in figure 5, the numerical solutions of the second-order Hamiltonian system (3.38) compare well with the third-order HOS model except for some minor discrepancies. From the comparison between the two results, it can be concluded that the second-order Hamiltonian system would serve as a reliable theoretical model.

Case	Ω (rad s^{-1})	K (rad m^{-1})	A (mm)	C (m s^{-1})	U_0 (m s^{-1})	ω_1 (rad s^{-1})	k_1 (rad m^{-1})	a_1 (mm)
I	1.61	6.30	7.6	0.26	2.10×10^{-4}	20.61	43.29	1.3
II	1.65	6.46	7.6	0.26	1.89×10^{-4}	$13.7 \leqslant \omega_1 \leqslant 28.0$	$19.1 \leqslant k_1 \leqslant 79.7$	1.3

TABLE 1. Dimensional parameters for the experiments of Lewis *et al.* (1974) with the density ratio $\rho_1/\rho_2 = 0.87$ and the depth ratio $h_1/h_2 = 10$. Ω: internal wave frequency. K: internal wavenumber. A: amplitude of internal wave. $C = \Omega/K$: internal wave phase speed. U_0: speed of surface current induced by the internal wave given by (5.4). ω_1: surface wave frequency. k_1: surface wavenumber. a_1: amplitude of surface wave. Notice that the values of k_1 were not given in Lewis *et al.* (1974), but are computed using the linear dispersion relation (2.1).

5. Modulation of short surface waves by long internal waves

5.1. *Previous experiments of Lewis, Lake & Ko (1974)*

The group resonance was studied experimentally by Lewis *et al.* (1974), who examined the slow modulation of a short surface wave with a small amplitude interacting with a long internal wave with a larger amplitude. The experiments were performed in a $0.9 \times 0.9 \times 12$ m tank filled with two fluids whose density ratio was $\rho_1/\rho_2 = 0.87$. The depths of the upper and lower fluid layers were $h_1 = 0.762$ m and $h_2 = 0.076$ m, respectively, giving a depth ratio of $h_1/h_2 = 10$. Monochromatic surface and internal waves propagating in the same direction were generated simultaneously in the tank and the resulting modulation of the free surface was examined. The surface and internal wave displacements were measured using two independent resistance gauges at several downstream locations over 10 m. In addition, an optical wave slope gauge was used to obtain slope estimates of the free surface.

As a measure of the local amplitude, a, and slope modulation, m, of the surface wave, Lewis *et al.* (1974) introduced the following fractional changes

$$a^* = \frac{a_{max} - a_{min}}{a_{max} + a_{min}}, \quad m^* = \frac{m_{max} - m_{min}}{m_{max} + m_{min}}, \tag{5.1a,b}$$

where the subscripts max and min represent maximum and minimum of the temporal measurements of the envelope amplitude and the wave slope at different locations. Notice that $0 \leqslant a^*, m^* \leqslant 1$ with $a \geqslant 0$ and $m \geqslant 0$. As a^* and m^* increase from zero with modulation, they are well suited to quantifying the amplitude and slope modulation of the surface wave and are measured experimentally as functions of the distance from the wavemaker, or x.

Lewis *et al.* (1974) performed two different experiments: cases I and II. For case I, an internal wave train with frequency Ω and a surface wave train with frequency ω_1 were generated. For the group resonance, the wave frequencies were chosen such that the phase speed of the internal wave, C, is close to the group velocity of the surface wave, c_g. Then the spatial evolutions of a^* and m^* were computed from temporal measurements of the surface elevation at a few different locations.

For case II, while an internal wave with a fixed value of Ω was generated, the surface wave frequency ω_1 was varied to identify the dependence of modulations on C/c_g. In particular, the question was if the maximum modulation occurs when $C/c_g = 1$, or the group resonance condition is met.

Physical parameters for the experiments are summarized in table 1. The data for cases I and II correspond to rows one and five in the table on page 780 in Lewis

Case	AK	a_1k_1	Kh_1	Kh_2	k_1h_1	C/c_g	U_0/C
I	0.048	0.055	4.80	0.48	33.0	1 ± 0.02	7.1×10^{-4}
II	0.048	$0.02 \leqslant a_1k_1 \leqslant 0.10$	4.93	0.49	$14.6 \leqslant kh_1 \leqslant 60.7$	$0.75 < C/c_g < 1.4$	6.9×10^{-4}

TABLE 2. Dimensionless parameters for the experiments of Lewis *et al.* (1974), where the density ratio $\rho_1/\rho_2 = 0.87$ and the depth ratio $h_1/h_2 = 10$ are fixed for both cases.

et al. (1974), respectively. The corresponding dimensionless parameters are listed in table 2. Notice that the wave steepnesses ($KA = 0.048$ and $k_1a_1 = 0.055$) are small, but are much greater than those of Alam (2012) discussed in §4.2, where $KA = 0.001$ and $k_1a_1 = 0.008$.

For $\rho_1/\rho_2 = 0.87$ and $h_1/h_2 = 10$, the critical wavenumber k_c can be computed as $k_ch_1 \simeq 20.924$ from (2.3) while the surface wavenumber for the group resonance k_g is given by $k_gh_1 \simeq 28.717$ from (2.6). It should be remarked that C/c_g for the values of Ω and ω_1 in Lewis *et al.* (1974) is approximately 0.932, which is different from 1 ± 0.02 in table 2. The source of this discrepancy is unclear, but we use values of C/c_g close to 1 in our numerical simulations, as described later.

5.2. *Linear modulation theory*

As the amplitude of the surface wave is much smaller than that of the internal wave ($a/A \simeq 0.17$), one can assume, at leading order, that the internal wave is little affected by the surface wave while the surface wave is modulated by a current induced by the internal wave. When the interface displacement can be approximated by a monochromatic internal wave so that

$$\zeta_2(x, t) = A \cos K(x - Ct), \tag{5.2}$$

the horizontal velocity U induced by the internal wave at the mean free surface can be approximated by

$$U(x, t) \approx \frac{1}{\rho_1} \frac{\partial \Psi_1}{\partial x} = -U_0 \cos K(x - Ct). \tag{5.3}$$

Using the linear relationship between Ψ_1 and ζ_2 given by (A 10) with (A 11) in appendix A, the current speed $U_0 > 0$ can be obtained as

$$U_0/C = \sigma KA, \quad \sigma = \frac{gK \operatorname{sech}(Kh_1)}{gK \tanh(Kh_1) - \Omega^2}. \tag{5.4a,b}$$

As U_0/C is proportional to the internal wave steepness, or $O(KA)$, one can assume $U_0/C \ll 1$ to be consistent with the experiment of Lewis *et al.* (1974).

When a surface wave train is modulated by a slowly varying surface current $U(x, t)$, it can be represented by

$$\zeta_1(x, t) = a(x, t)\, e^{i\theta(x,t)}, \tag{5.5}$$

where $a(x, t)$ is the amplitude of the envelope varying slowly in space and time while $\theta(x, t)$ is the phase function. The local wavenumber $k(x, t)$ and the local wave

frequency $\omega(x, t)$ can be found as $k = \partial\theta/\partial x$, and $\omega = -\partial\theta/\partial t$, respectively. Then, the slowly varying k and ω satisfy the kinematic wave conservation equation

$$\frac{\partial k}{\partial t} + \frac{\partial \omega}{\partial x} = 0. \tag{5.6}$$

As relatively short surface waves are of interest, one can assume $kh_1 \gg 1$ so that the short surface waves satisfy the linear dispersion relation for infinitely deep water, which is given, in the presence of a slowly varying current $U(x)$ induced by a long internal wave, by

$$\omega = (gk)^{1/2} + kU. \tag{5.7}$$

Substituting (5.7) into (5.6) then yields

$$\frac{\partial k}{\partial t} + (c_g + U)\frac{\partial k}{\partial x} = -k\frac{\partial U}{\partial x}, \tag{5.8}$$

where $c_g(k)$ is the group velocity of the surface wave given by $c_g = \frac{1}{2}(g/k)^{1/2}$.

When short surface waves propagate over a non-uniform current, their energy is not conserved. Instead, the wave action defined by $E/(gk)^{1/2}$ is conserved (Bretherton & Garrett 1969), from which the energy density E of the surface wave is governed by

$$\frac{\partial E}{\partial t} + \frac{\partial}{\partial x}[(c_g + U)E] = -\frac{1}{2}E\frac{\partial U}{\partial x}, \tag{5.9}$$

where the right-hand side of (5.9) represents the radiation stress in the direction of the wave field (Longuet-Higgins & Stewart 1960, 1961; Whitham 1962). Under the small wave steepness assumption, as E is proportional to a^2, the evolution equation for $a(x, t)$ can be obtained, from (5.9), as

$$\frac{\partial a^2}{\partial t} + (c_g + U)\frac{\partial a^2}{\partial x} = -\frac{3}{2}a^2\frac{\partial U}{\partial x} - a^2\frac{\partial c_g}{\partial x}. \tag{5.10}$$

It should be pointed out that the system for $k(x, t)$ and $a(x, t)$ given by (5.8) and (5.10) can be obtained from the Hamiltonian system (3.38) by taking an appropriate limit and, therefore, the linear modulation theory is contained in our numerical model. Although the exact decomposition of the surface and interface displacements into the barotropic and baroclinic modes should be made in the spectral space, as described in Choi *et al.* (2020), it can be shown from (3.38) that the evolution of the barotropic components of ζ_1 and Ψ_1 can be approximated, using a small parameter associated with the slow variation of a baroclinic current U (specifically, $K/k_1 \ll 1$), by

$$\frac{\partial \zeta_1}{\partial t} = \Gamma_{11}[\Psi_1] - \frac{\partial(U\zeta_1)}{\partial x}, \quad \frac{\partial \Psi_1}{\partial t} = -\rho_1 g\zeta_1 - U\frac{\partial \Psi_1}{\partial x}. \tag{5.11a,b}$$

Here, $U(x, t)$ is the surface current given by (5.3) that is assumed to vary slowly in space and time, and the Fourier multiplier for Γ_{11} acting on the barotropic component, or short surface waves, is approximated by $\gamma_{11} = |k|/\rho_1$. Then, substituting (5.5) for ζ_1 and a similar expression of Ψ_1 into (5.11) yields, at the leading-order approximation for small K/k_1, the evolution equations for $a(x, t)$ and $k(x, t)$ given by (5.8) and (5.10) (Choi & Lyzenga 2006).

As shown in Lewis *et al.* (1974), equations (5.8) and (5.10) can be solved using the method of characteristics when they are written as

$$\frac{\mathrm{d}k}{\mathrm{d}\tau} = -k\frac{\partial U}{\partial x}, \tag{5.12}$$

$$\frac{\mathrm{d}a^2}{\mathrm{d}\tau} = -\frac{3}{2}a^2\frac{\partial U}{\partial x} - a^2\frac{\partial c_g}{\partial x}, \tag{5.13}$$

where the characteristic curves are given by

$$\frac{\mathrm{d}x}{\mathrm{d}\tau} = c_g + U, \quad \frac{\mathrm{d}t}{\mathrm{d}\tau} = 1. \tag{5.14a,b}$$

To obtain closed-form solutions of (5.12)–(5.13), Lewis *et al.* (1974) adopted an asymptotic approach assuming $U_0/C = O(KA) \ll 1$ from (5.4) or, equivalently, $U_0/c_g \ll 1$ with $C/c_g = O(1)$ for the group resonance. While Lewis *et al.* (1974) obtained an asymptotic solution in terms of the Heaviside function, which corresponds to imposing the boundary condition at the wavemaker, we here use an asymptotic solution of the initial value problem for (5.12)–(5.14) for the spatially periodic current given by (5.3) for its comparison with the numerical solutions of the Hamiltonian system (3.38). The explicit asymptotic solutions are given in appendix B.

At group resonance ($C = c_g$), the solutions of (5.12)–(5.14) for $k(x, t)$ and $a(x, t)$ valid to $O(\epsilon)$ can be reduced, from (B 12)–(B 13), to

$$k(x, t) = k_0 \exp(-U_0 K t \sin \theta_1), \tag{5.15}$$

$$a(x, t) = a_0 \exp\left[-\tfrac{3}{4}U_0 K t \sin \theta_1 - \tfrac{1}{8}U_0 C (Kt)^2 \cos \theta_1\right], \tag{5.16}$$

where $\theta_1 = K(x - Ct)$. Then, the maxima and minima of a and k at a fixed time are given by

$$k_{max,min} = k_0 \exp\left[\pm(U_0/C)(\Omega t)\right], \tag{5.17}$$

$$a_{max,min} = a_0 \exp\left[\pm\tfrac{3}{4}(U_0/C)(\Omega t)\left(1 + \tfrac{2}{72}(\Omega t)^2\right)^{1/2}\right], \tag{5.18}$$

where $\Omega = KC$ has been used and the plus and minus signs are chosen for the maxima and minima, respectively. Based on the linear modulation theory, both $|k_{max,min}|$ and $|a_{max,min}|$ increase with t. Then a^* and m^* defined by (5.1) with $m = ka$ can be found as

$$a^*(t) = \tanh[\tfrac{3}{4}(U_0/C)(\Omega t)(1 + \tfrac{1}{36}(\Omega t)^2)^{1/2}], \tag{5.19}$$

$$m^*(t) = \tanh[\tfrac{7}{4}(U_0/C)(\Omega t)(1 + \tfrac{1}{196}(\Omega t)^2)^{1/2}], \tag{5.20}$$

which are independent of the initial surface wave parameters and depend only on the internal wave steepness since $U_0/C = \sigma KA$, as shown in (5.4). While k and a increase in time exponentially, $a^*(t)$ and $m^*(t)$ approach 1 as $t \to \infty$.

For small t, or $\Omega t \ll 1$, $a^*(t)$ and $m^*(t)$ can be approximated by

$$a^*(t) \simeq \tfrac{3}{4}(U_0/C)(\Omega t), \quad m^*(t) \simeq \tfrac{7}{4}(U_0/C)(\Omega t). \tag{5.21a,b}$$

Therefore, for small Ωt, or equivalently, small Kx with $x = Ct$, both $a^*(t)$ and $m^*(t)$ grow linearly in time and the growth rates increase with the internal wave steepness.

In fact, Lewis *et al.* (1974) noticed that the experimental data for different physical parameters collapse when $a^*/(U_0/C)$ and $m^*/(U_0/C)$ are used. This shows that their measurements were made over a relatively short distance or short time.

The exponential growths of $a(x, t)$ and $k(x, t)$ in time given by (5.15)–(5.16) are the result of the linear modulation theory for surface waves without considering the energy exchange with the internal wave. Therefore, the solutions given by (5.15)–(5.16) would be valid for $\Omega t \ll O(1/\epsilon)$. As time increases so that $\Omega t = O(1/\epsilon)$, the energy exchange through near-resonant triad interactions becomes important and the linear modulation theory is expected to less accurately describe the evolution of $a(x, t)$ and $k(x, t)$.

Another interesting feature in question is the location of the rough sea surface relative to the phase of the internal wave. Previously, its exact location for the long internal wave or the internal solitary wave has not been well understood as different field observations have been made (Gasparovic *et al.* 1988; Watson & Robinson 1990; Hwung *et al.* 2009).

From (5.15)–(5.16), the local wave steepness $m = ka$ is given by

$$m(x, t) = m_0 \exp[\tfrac{7}{4}(U_0/C)(\Omega t)(1 + \tfrac{1}{196}(\Omega t)^2)^{1/2} \ \cos(\theta_1 - \varphi)], \qquad (5.22)$$

where $m_0 = k_0 a_0$, and φ is defined as

$$\varphi = \tan^{-1}\left(\frac{6}{\Omega t}\right) + \pi, \qquad (5.23)$$

which yields $\varphi = 3\pi/2$ for small t and $\varphi = \pi$ for large t. Then, from (5.22), as the maximum surface wave steepness is observed at $\theta_1 = \varphi$, its location can be found initially at up-crossings behind the crests of the internal wave, or at the points where the surface current given by (5.3) converges. On the other hand, as t increases, the location of the maximum surface wave steepness is expected to be right above the internal wave troughs. Therefore, under the group resonance condition, steep surface waves are expected to appear at a point where the surface current converges only for a relatively short interaction period, but eventually appear right above the wave troughs. This conclusion, based on the linear modulation theory, will be further discussed later with the numerical solutions of the nonlinear Hamiltonian system.

6. Numerical solutions compared with the experiment

When the internal wave characteristics (K, Ω) are used to non-dimensionalize physical variables, $a^*(t)$ and $m^*(t)$ are functions of the following dimensionless parameters

$$(a^*, m^*) = f(\Omega t, \ k_1/K, \ Ka_1, \ KA, \ Kh_1, \ Kh_2, \ \rho_1/\rho_2). \qquad (6.1)$$

Under the group resonance condition $(c_g = C)$, the ratio between the surface and internal wavenumbers k_1/K is fixed and can be dropped from (6.1). Then, an alternative form of (6.1) is given by

$$(a^*, m^*) = f(\Omega t, \ k_1 a_1, \ KA, \ Kh_1, \ h_1/h_2, \ \rho_1/\rho_2). \qquad (6.2)$$

Equation (6.2) identifies the dimensionless parameters involved for the surface wave modulation under group resonance. As shown in (5.21), at the early stage of surface modulation, both a^* and m^* are independent of the surface wave steepness $\epsilon_S = k_1 a_1$ and depend linearly on the internal wave steepness $\epsilon_I = KA$ for fixed values of the remaining parameters. In the simulations presented hereafter, following Lewis *et al.* (1974), we use fixed values of $\epsilon_S = 0.055$ and $Kh_1 = 4.8$, but vary ϵ_I, h_1/h_2 and ρ_1/ρ_2.

6.1. *Initialization for the experiment of Lewis, Lake & Ko (1974)*

After employing $h_1/h_2 = 10$ and $\rho_1/\rho_2 = 0.87$, the same as those in the experiment of Lewis *et al.* (1974), we assume that the internal wave is a monochromatic wave (5.2) with $Kh_1 = 4.8$. Due to the periodic boundary conditions used in the pseudo-spectral method, a surface wavenumber identical to that used in the experiment is not admissible. As an integer number of surface wavelengths must be employed within an internal wavelength, the wavenumber of the initial monochromatic surface wave can be written as

$$k_1 = \kappa K, \tag{6.3}$$

where κ is an integer.

For case I, we choose $\kappa = 6$ so that the surface wavenumber $k_1 h_1 = 28.8$, which is close to the wavenumber for group resonance, $k_g h_1 \simeq 28.717$. Then, $C/c_g \simeq 1.009$. In comparison with $C/c_g = 1 \pm 0.02$ in Lewis *et al.* (1974), our choice of $\kappa = 6$ gives k_1, which is within the error estimate of the experiment. For case II, $\kappa = 2$–14, giving a range of ratios for C/c_g in the experiment.

In our numerical simulations, we use wave steepnesses identical to those used in the experiments: $\epsilon_S = 0.055$ and $\epsilon_I = 0.048$. While ϵ_S and ϵ_I are comparable, the amplitude of the internal wave is much greater than that of the surface wave: $A/a_1 \simeq 5.24$. The initial conditions for ζ_1 and ζ_2 are given by a linear superposition of the surface (barotrophic) and internal (baroclinic) wave modes so that

$$\zeta_1 = a_1 \cos(k_1 x) + \beta_3^- A \cos(Kx), \quad \zeta_2 = \alpha_3^+ a_1 \cos(k_1 x) + A \cos(Kx), \tag{6.4a,b}$$

where $\alpha_3^+ = \alpha_3(k_1, \omega_1)$ and $\beta_3^- = \beta_3(K, \Omega)$ with α_3 and β_3 given by (A 9) and (A 11), respectively. For the physical parameters in the experiment, $\alpha_3^+ \approx 0$ and $\beta_3^- = -7.18 \times 10^{-4}$. Therefore, it can be safely assumed that the surface and interface displacements represent mostly those from the surface and internal wave modes, respectively. In addition, the linear relations in appendix A are used for Ψ_1 and Ψ_2.

The computational domain length and time are chosen to be sufficiently large for short surface waves to be fully evolved, typically, 5Λ and $12T$, respectively, where $\Lambda = 2\pi/K$ and $T = 2\pi/\Omega$ are the wavelength and period of the internal wave, respectively. Convergence tests are performed for different choices of the computational domain length L and the number of grid points per surface wavelength M_{ζ_1} and their results will be discussed in §6.2. The time step Δt is chosen such that the Courant–Friedrichs–Lewy conditions are met: $c_1 \Delta t/\Delta x \ll 1$ and $C \Delta t/\Delta x \ll 1$, where $\Delta x = L/M$ while $c_1 = \omega_1/k_1$ and $C = \Omega/K$ are the phase speeds of the surface and internal waves, respectively.

As the numerical model solves initial value problems with periodic boundary conditions, it computes the temporal evolution of the surface and internal waves. For comparison with the measurements of a^* and m^*, the temporal evolution of the surface wave envelope needs to be transformed to the corresponding spatial evolution, or *vice versa*. Here, the transformation with the group velocity of the surface wave is adopted, i.e. $x = c_g t$, and the interaction distance measured with respect to K becomes $Kx = Kc_g t = KCt = \Omega t$ when $C/c_g = 1$.

6.2. *Comparison with experiments of Lewis et al. (1974)*

Figure 6 shows the time evolution of the surface and internal wave displacements for case I. From figure 6(a), it is observed that the simulated surface wave is modulated by the internal wave and evolves into almost spatially periodic wave packets. When it
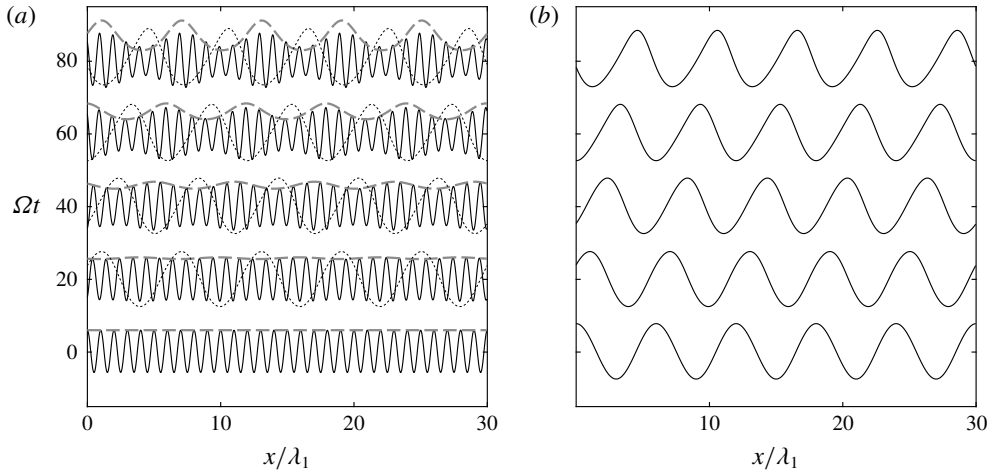
FIGURE 6. Snapshots of (*a*) surface (ζ_1) and (*b*) interface (ζ_2) displacements for case I with $C/c_g \simeq 1$. Solid curves: simulated wave displacements. Dashed curves: theoretical upper wave envelope from (5.16) in § 4. Dotted curves: the interface displacements shown in (*b*) to display the relative phase between the surface and interface displacements. Notice that the vertical scales of the surface and interface displacements are different. At $t = 0$ the amplitude ratio between the surface and internal wave modes is $A/a_1 = 5.24$. The horizontal axis is given by x/λ_1, where λ_1 is the surface wavelength.

is compared with the numerical solution, the linear modulation theory in § 5.2 predicts accurately the amplitude of the envelope, but, for instance, around $\Omega t \approx 80$, starts to overpredict the surface modulation. From figure 6(*b*), a slight change in the internal wave profile is observed relative to the initial profile. Slightly steep crests and flattened troughs are observed. This change could be attributed to the effect of the second-order nonlinearity in the Hamiltonian system on the internal wave. This nonlinear behaviour seems to appear due to the shallowness of the lower layer, where the dimensionless internal wavenumber $Kh_2 = 0.48$ or $h_2/\Lambda = 0.076$. In the simulations for larger values of Kh_2, the internal wave of the same steepness shows little changes in its profile.

As shown in figure 6(*a*), the maximum surface wave steepness is observed approximately right above the internal wave troughs. This is consistent with the theoretical prediction discussed in § 5.2. Therefore, while the linear modulation theory starts to deviate from the numerical solution (and the observation) at $\Omega t \approx 80$, it predicts well the location of steep surface area.

Figure 7 shows the numerical results for the amplitude modulation a^* given by (5.1) as a function of Ωt for varying two numerical parameters: M_{ζ_1} and L, which are the number of spatial grid points per surface wavelength and the computational domain length, respectively. The numerical data for a^* are shown scattered for fixed values of M_{ζ_1} and L. For the convergence test, the scattered numerical results are smoothed with 50 iterations of a three-point moving average. The solid black and grey curves show smoothed numerical data for various choices of M_{ζ_1} and L. This convergence test shows that the choice of $M_{\zeta_1} = 32$ and $L = 5\Lambda$, employed in figure 6, is sufficient to capture the amplitude modulation described by a^*.

Figure 8 shows the amplitude a^* and slope m^* modulations for case I, as functions of Ωt, from the experiment, simulation and linear modulation theory. The experimental data shown by open circles are extracted from figures 12 and 13
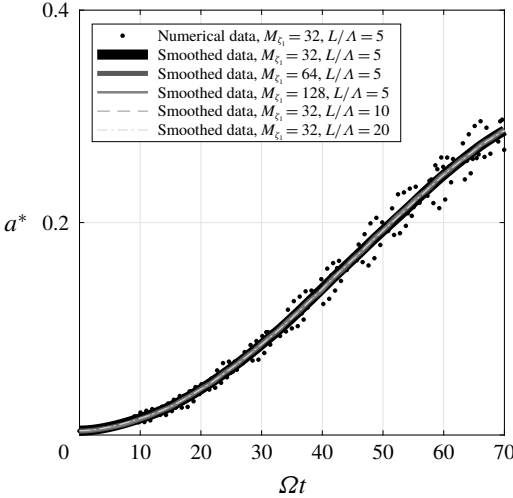
FIGURE 7. Convergence of amplitude modulation, a^*, as a function of Ωt for case I for different values of the number of spatial grid points per surface wavelength M_{ζ_1} and the computational domain length L. The numerical data (dots) are smoothed with 50 iterations of a three-point moving average.
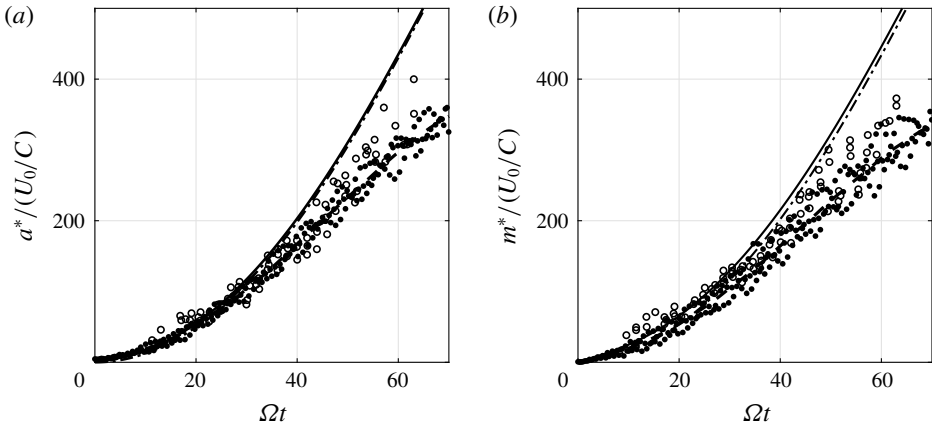

FIGURE 8. Normalized amplitude and slope modulation, a^* and m^* defined by (5.1), as functions of Ωt for case I. Open circles: experiment; dots: simulation employing $\kappa = 6$ in (6.3); dashed curves: smoothed numerical solutions; solid curves: linear modulation theory of Lewis *et al.* (1974) given by (B 15)–(B 16); dash–dotted curves: linear modulation theory given by (5.19)–(5.20).

on page 796 in Lewis *et al.* (1974) and are normalized by U_0/C. As shown in (5.21), this normalization makes their experimental data for different physical parameters collapse almost onto a single curve over a short interaction distance or time. The two theoretical solutions discussed in appendix B, corresponding to those of the boundary and initial value problems, respectively, are also presented, but show little difference. This confirms that the transformation from the temporal evolution of the surface wave
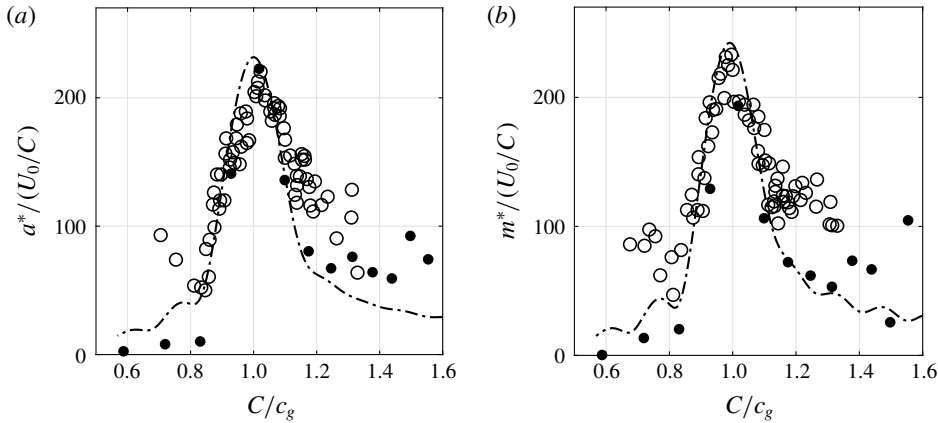
FIGURE 9. Normalized amplitude and slope modulation, a^* and m^*, from (5.1) as functions of C/c_g at $Kx = \Omega t = 43$ for case II. Open circles: experiment; dots: simulations employing $\kappa = 2\text{--}14$ in (6.3); dash–dotted curves: linear modulation theory given by (B 12)–(B 13).

to the spatial evolution using its group velocity is reliable. Therefore, hereafter, only the asymptotic solutions in § 5.2 will be presented.

As shown in figure 8, the experimental and numerical data are in good agreement, although relatively minor discrepancies are observed. On the other hand, the linear modulation theory agrees with the experimental and numerical data approximately up to $\Omega t = 30$, but clearly overestimates the surface wave modulation approximately for $\Omega t > 40$. This observation indicates that the linear modulation theory fails to describe the modulation after the initial exponential growth and needs to be modified to include nonlinear effects, as discussed in the following section.

To investigate how effective the group resonance mechanism is for the modulation of short surface waves, we numerically study case II of Lewis *et al.* (1974). Figure 9 shows a^* and m^* as functions of C/c_g at a fixed propagation distance of $Kx = \Omega t = 43$, chosen in their experiment. The experimental data are extracted from figures 14 and 15 on page 797–798 in Lewis *et al.* (1974). From figure 9, it is observed experimentally, numerically and theoretically that the largest amplitude and slope modulation appear under the group resonance condition, $C/c_g = 1$. Notice that, due to the periodic boundary conditions of our numerical model, only a few data points are available through $\kappa = 2\text{--}14$ in (6.3). Nevertheless, the limited numbers of data points reveal the trend of the experiment and theory.

6.3. *Evolution of surface waves over a longer period*

Figure 10 shows a^* and m^* as functions of Ωt for case I for a longer period than that displayed in figure 8. It is observed that, after the initial exponential growth, the modulation reaches a maximum at $\Omega t \approx 90$ before it starts to oscillate. This implies that the k_1 wave is modulated and starts to exchange energy with its sidebands through near-resonant wave interactions, as discussed in Alam (2012). In Lewis *et al.* (1974), as the measurements were made over a short distance, the initial growth of sidebands were reasonably well described by the linear modulation theory and no energy flow back to the carrier wave was observed.
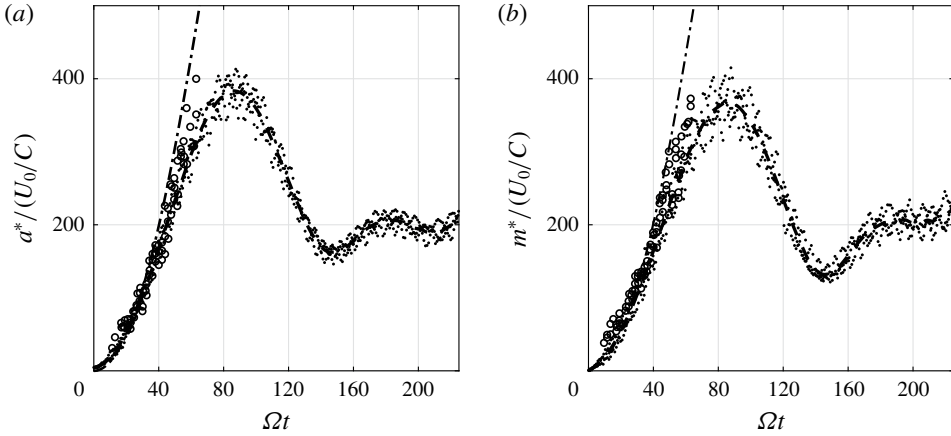
FIGURE 10. Normalized amplitude and slope modulation, a^* and m^* defined by (5.1), as functions of Ωt for case I for a longer period than the experiment of Lewis *et al.* (1974). Open circles: experiment; dots: simulation employing $\kappa = 6$ in (6.3); dashed curves: smoothed numerical solutions; dash–dotted curves: linear modulation theory given by (5.19)–(5.20).
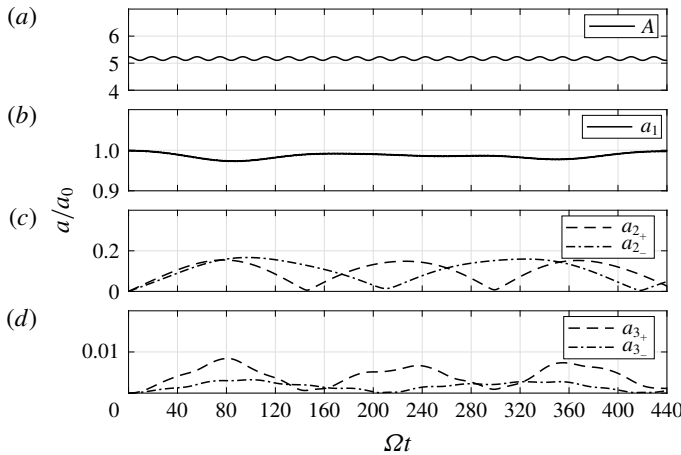

FIGURE 11. Numerical solutions of the Hamiltonian system for the amplitudes of surface and internal waves for internal wave steepness $\epsilon_I = 0.048$ corresponding to case I of the experiments. (*a*) Internal wave amplitude A. (*b*) Surface wave amplitude a_1. (*c,d*) Near-resonant surface wave amplitudes a_{n+} (dashed curves) and a_{n-} (dash–dotted curves) for $n = 2, 3$. The amplitudes are normalized by the initial surface wave amplitude $a_0 = a_1(t = 0)$.

Figure 11 shows the time evolution of A, a_1 and $a_{n\pm}$ ($n = 2, 3$) that are the wave amplitudes of wavenumbers K, k_1 and $k_{n_\pm} = k_1 \pm (n - 1)K$. These amplitudes are computed from the moduli of the numerical surface and interface displacements $|\hat{\zeta}_1(k, t)|$ and $|\hat{\zeta}_2(k, t)|$, respectively, which have been shown to be good approximations to the amplitudes of the surface and internal wave modes, as pointed out in (6.4). The amplitudes are normalized by the initial amplitude of the surface wave $a_0 = a_1(t = 0)$ of ζ_1.

From figure 11(*a*), the internal wave amplitude A whose magnitude is approximately 5 times higher than a_1 is observed to oscillate with a relatively small amplitude. While the source of this oscillation of a relatively short period (but much greater than $2\pi/\Omega$) is unclear, it seems to be the effect of the shallow lower layer ($Kh_2 = 0.48$) as the simulations with deeper lower layers do not exhibit such an oscillation. Unfortunately, no measurements of internal waves were reported in Lewis *et al.* (1974).

In the meantime, it is observed from figure 11(*b*) that a_1 also oscillates with a small amplitude, but with a much longer period than the oscillation period of A. Initially a_1 decreases and reaches its minimum around $\Omega t \approx 90$ indicating that energy is transferred to neighbouring wave components that satisfy the near-resonant conditions. As can be seen from figure 11(*c*), $a_{2_\pm}$, which are the third members of the primary resonant triads, receive energies from the waves of A and a_1 to grow from zero and then decay by returning their energies back to a_1 and A. This process repeats with distinct recurrence periods: $\Omega t \approx 150$ for a_{2_+} and $\Omega t \approx 210$ for a_{2_-}. When $a_{2_\pm}$ are close to their maxima around $\Omega t \approx 90$, the surface wave modulation measured by a^* and m^* reaches its maximum, as shown in figure 10. Similarly to Alam (2012), $a_{3_\pm}$ are also excited by successive interactions, but their amplitudes observed in figure 11(*d*) are much smaller than those of the primary resonant triads, e.g. approximately one order of magnitude smaller than $a_{2_\pm}$.

Unlike the resonant interaction studied by Alam (2012) (also considered in § 4.2), the interactions are relatively weak for the parameters used in the experiment of Lewis *et al.* (1974). For example, the variation of the amplitude of the k_1 wave during the primary triad interaction with $k_{2_\pm}$ is much smaller than that observed in Alam (2012). Furthermore the amplitudes of the sidebands excited by the successive interactions ($k_{n_\pm}$ for $n \geqslant 3$) are much smaller than those in Alam (2012). Although they are necessary to accurately describe the surface wave field, the sidebands excited by successive interactions are less important for the parameters in the experiment of Lewis *et al.* (1974).

7. Discussion

7.1. *Amplitude equations for group resonance*

When an internal wave train of wavenumber K co-exists with a surface wave train of k_1 that is equal or close to k_g, it has been shown that the surface wave is modulated by a non-uniform surface current induced by the internal wave. In particular, the description of the two primary triads (k_1, k_{2_-}, K) and (k_1, k_{2_+}, K) seems to be critical.

When the amplitudes of the k_j and K waves are denoted by a_j and A, respectively, it is well known that their time evolution can be studied by a system of amplitude equations. In Choi *et al.* (2020), such a system for two-layer flows is obtained in terms of complex conjugate variables $\mathcal{A}_j$ and $\mathcal{B}_0$, which are related approximately to the real amplitudes a_j and A as

$$a_j(t) \approx \sqrt{\frac{2}{\omega_j}} |Q_j^{(1,1)}| \, |\mathcal{A}_j|, \quad A(t) \approx \sqrt{\frac{2}{\Omega}} |Q_0^{(2,2)}| \, |\mathcal{B}_0|, \quad (7.1a,b)$$

where $Q_j^{(m,n)} = Q^{(m,n)}(k_j)$ are real-valued functions depending on the wavenumber and physical parameters (density and depth ratios), as listed in appendix C. These relationships are found by assuming that the surface and interface displacements approximately represent the amplitudes of the barotropic and baroclinic modes as the leading-order approximation.

Then, the amplitude equations for surface ($\mathcal{A}_1$, $\mathcal{A}_{2_\pm}$) and internal ($\mathcal{B}_0$) wave modes are given by

$$\frac{\mathrm{d}\mathcal{A}_1}{\mathrm{d}t} = \mathrm{i}\,V_{1,2_-,0}^{(2)}\,\mathcal{A}_{2_-}\,\mathcal{B}_0\,\mathrm{e}^{-\mathrm{i}\delta_- t} + \mathrm{i}\,V_{2_+,1,0}^{(2)}\,\mathcal{A}_{2_+}\,\mathcal{B}_0^*\,\mathrm{e}^{\mathrm{i}\delta_+ t}, \tag{7.2a}$$

$$\frac{\mathrm{d}\mathcal{A}_{2_-}}{\mathrm{d}t} = \mathrm{i}\,V_{1,2_-,0}^{(2)}\,\mathcal{A}_1\,\mathcal{B}_0^*\,\mathrm{e}^{\mathrm{i}\delta_- t}, \qquad \frac{\mathrm{d}\mathcal{A}_{2_+}}{\mathrm{d}t} = \mathrm{i}\,V_{2_+,1,0}^{(2)}\,\mathcal{A}_1\,\mathcal{B}_0\,\mathrm{e}^{-\mathrm{i}\delta_+ t}, \tag{7.2b}$$

$$\frac{\mathrm{d}\mathcal{B}_0}{\mathrm{d}t} = \mathrm{i}\,V_{1,2_-,0}^{(2)}\mathcal{A}_1\mathcal{A}_{2_-}^*\,\mathrm{e}^{\mathrm{i}\delta_- t} + \mathrm{i}V_{2_+,1,0}^{(2)}\mathcal{A}_1^*\mathcal{A}_{2_+}\,\mathrm{e}^{\mathrm{i}\delta_+ t}, \tag{7.2c}$$

where the expressions for the interaction coefficients $V_{1,2_\pm,0}^{(2)} = V^{(2)}(k_1, k_{2_\pm}, K)$ can be found in appendix C. Notice that the amplitude equations for exact resonance have been modified to describe near-resonant interactions by multiplying the exponential functions with δ_- and δ_+, which are detuning parameters from exact resonance defined as

$$\delta_- = \omega_1 - \omega_{2_-} - \Omega, \qquad \delta_+ = -\omega_1 + \omega_{2_+} - \Omega. \tag{7.3a,b}$$

While it is not written explicitly, the system given by (7.2) describes the evolution of the slowly varying wave amplitudes that depend on the slow time ϵt with ϵ being the wave steepness, which could be either ϵ_I or ϵ_S with $\epsilon_I = O(\epsilon_S)$. In addition, $\delta_\pm/\omega_1 = O(\epsilon)$ has been assumed for near-resonant interactions.

For the experiment of Lewis *et al.* (1974), the wavenumbers and frequencies of the primary triads are

$$(k_1, k_{2_-}, K) = (28.8, 24.0, 4.8)/h_1, \qquad (\omega_1, \omega_{2_-}, \Omega) \simeq (5.367, 4.899, 0.448)/(g/h_1)^{1/2}, \tag{7.4a}$$

$$(k_1, k_{2_+}, K) = (28.8, 33.6, 4.8)/h_1, \qquad (\omega_1, \omega_{2_+}, \Omega) \simeq (5.367, 5.797, 0.448)/(g/h_1)^{1/2}, \tag{7.4b}$$

which yield $\delta_- \sim 0.020/(g/h_1)^{1/2}$ and $\delta_+ \sim -0.018/(g/h_1)^{1/2}$. Using the expressions presented in appendix C, the interaction coefficients in (7.2) are computed as

$$V_{1,2_-,3}^{(2)} \simeq 0.265, \qquad V_{2_+,1,3}^{(2)} \simeq 0.314, \tag{7.5a}$$

while the transformations given by (7.1) become

$$a_1(t) \approx 3.512|\mathcal{A}_1|, \quad a_{2_-}(t) \approx 3.356|\mathcal{A}_{2_-}|, \quad a_{2_+}(t) \approx 3.650|\mathcal{A}_{2_+}|, \quad A(t) \approx 2.624|\mathcal{B}_0|, \tag{7.6a-d}$$

where we have used the computed values of $Q_1^{(1,1)} \simeq 5.754$, $Q_{2_-}^{(1,1)} \simeq 5.252$, $Q_{2_+}^{(1,1)} \simeq 6.215$ and $Q_0^{(2,2)} \simeq -1.242$.

From $k_1 a_1(0) = \epsilon_S (= 0.055)$ and $KA(0) = \epsilon_I (= 0.048)$ with $k_1 h_1 = 28.8$ and $Kh_1 = 4.8$, the initial wave amplitudes are found $a_1(0)/h_1 \simeq 1.91 \times 10^{-3}$ and $A(0)/h_1 \simeq 1.0 \times 10^{-2}$, which yield, from (7.1), $\mathcal{A}_1(0) \simeq 5.43 \times 10^{-4}$ and $\mathcal{B}_0(0) \simeq -3.81 \times 10^{-3}$ while $\mathcal{A}_{2_\pm}(0) = 0$.

For small t, one can show from (7.2b) that $\mathcal{A}_{2_\pm}$ grow linearly in t so that $a_{2_\pm}(t)$ are given by

$$a_{2_-}/a_0 \simeq 2.16 \times 10^{-3}\Omega t, \qquad a_{2_+}/a_0 \simeq 2.77 \times 10^{-3}\Omega t, \tag{7.7a,b}$$

where $a_0 = a_1(0)$. The estimated linear growth rates from the numerical solutions shown in figure 11 are approximately 2.3×10^{-3} and 2.8×10^{-3} for a_{2_-}/a_0 and a_{2_+}/a_0, respectively, which are in good agreement with the theoretical predictions in (7.7).
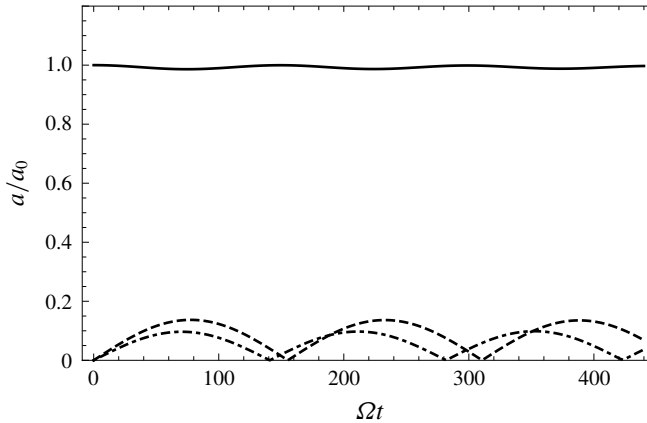
FIGURE 12. Numerical solutions of the amplitude equations given by (7.2) for the time evolution of the surface wave amplitudes for case I. Solid: $a_1(t)$; dashed: $a_{2_+}(t)$; dash–dotted: $a_{2_-}(t)$. The amplitude of the internal wave shows little change from its initial value and is not shown here. The amplitudes are normalized by the initial amplitude $a_0 = a_1(t = 0)$.

Figure 12 shows the numerical solution of the amplitude equations given by (7.2). The recurrence period of a_{2_-} is different from that in the numerical solution of the Hamiltonian system for a_{2_-} shown in figure 11. The cause of this difference is unclear, but could be attributed to the assumption that the surface displacement can be approximated only by the amplitude of the barotropic mode as the density difference between the two fluids is non-negligible. Nevertheless, considering that we only describe the primary triad interactions, the comparison between the two numerical solutions for surface waves is reasonable, for example, in terms of the amplitudes of $a_{2_\pm}$.

It should be stressed that the exponential functions with $\delta_\pm$ in (7.2) are crucial to describe near-resonant wave interactions. If $\delta_\pm = 0$ are used, the solutions of the amplitude equations would be so different from those of the Hamiltonian system. The numerical solution of the amplitude equations for the internal wave amplitude shows no short-period oscillation observed in figure 11 and remain almost constant. As mentioned previously, the oscillation of the internal wave might result from its own nonlinear effect amplified by the shallowness of the lower layer, which cannot be described by the amplitude equations given by (7.2).

7.2. *Realistic oceanic condition*

Simulations were performed with a density ratio close to one, $\rho_1/\rho_2 = 0.99$, for a realistic oceanic condition. The depth ratio is chosen to be $h_1/h_2 = 1/2$ so that the thickness of the lower layer is greater than that of the upper layer. In the experiment of Lewis *et al.* (1974), the density and depth ratios were $\rho_1/\rho_2 = 0.87$ and $h_1/h_2 = 10$, respectively. The internal wave is assumed to have the same wavelength as before, so that $Kh_1 = 4.8$ and $Kh_2 = 2Kh_1$. Therefore, the internal wavelength is comparable to both the upper and lower layer thicknesses for the condition of long waves. For this internal wavenumber, the resonance condition of $C/c_g = 1.0025$ yields $\kappa = k_1/K = 50$ in (6.3). This implies that the wavelength of a surface wave at group resonance is 50 times smaller than the internal wavelength. Furthermore, the waves to be excited
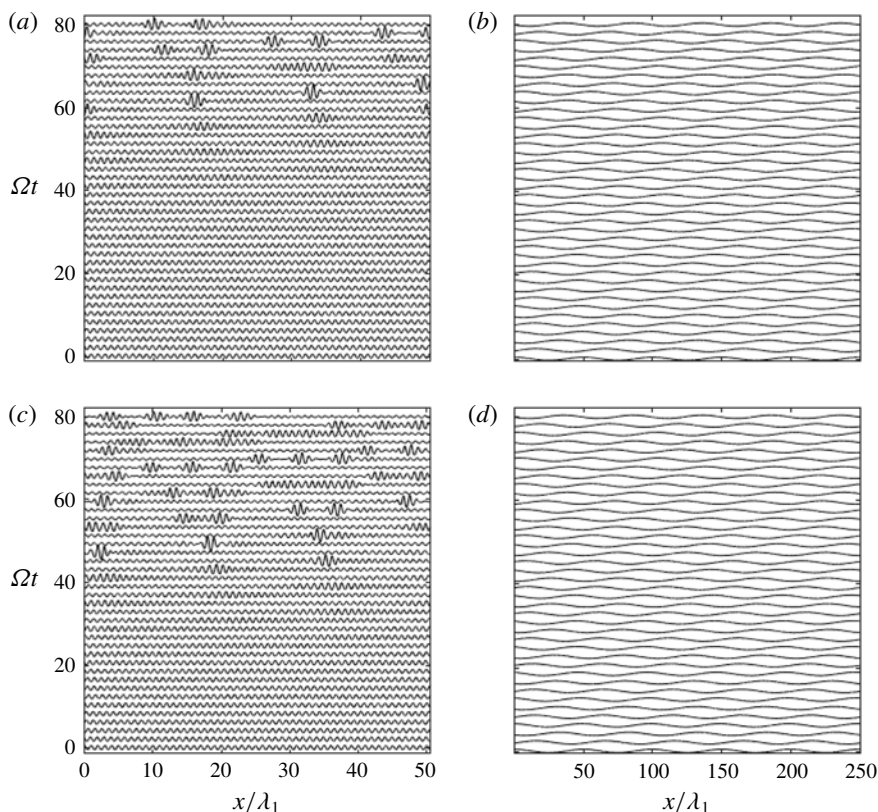
FIGURE 13. Numerical solutions for the time evolution of surface and interface displacements with realistic parameters $\rho_1/\rho_2 = 0.99$ and $h_1/h_2 = 1/2$. The surface wave steepness is fixed as $\epsilon_S = 0.06$ while two different internal wave steepnesses ϵ_I are used. (*a,c*) Surface wave displacements. (*b,d*) Internal wave displacements. (*a,b*) $\epsilon_I = 0.05$; (*c,d*) $\epsilon_I = 0.10$. The internal wave amplitudes shown in (*b*) and (*d*) are 25 and 45 times larger than the surface wave amplitudes in (*a*) and (*c*), respectively. Notice that the surface displacement is shown over one internal wavelength while the interface displacement is shown over the whole computational domain.

by successive near-resonant interactions would have wavenumbers close to k_1. For example, $k_{2\pm} = k_1 \pm K = k_1(1 \pm K/k_1) \approx k_1$ with $K/k_1 = 1/50 \ll 1$.

Figure 13 shows the surface and interface displacements for surface wave steepness $\epsilon_S = 0.06$ and two different internal wave steepnesses $\epsilon_I = 0.05$ and 0.1. Figures 13(*a,b*) and 13(*c,d*) correspond to $\epsilon_I = 0.05$ and 0.10, respectively. Figures 13(*a,c*) and 13(*b,d*) show the surface and interface displacements, respectively. Due to the scale separation between the two wave fields, while the entire wave field covering five wavelengths (5Λ) is displayed for the internal wave, the surface wave field is shown over only one internal wavelength ($\Lambda = 50\lambda_1$) to better observe the surface wave field.

Compared with the experiment of Lewis *et al.* (1974) with a shallow lower layer, when the lower layer depth is increased, the monochromatic internal wave field experiences little change throughout the evolution regardless of the steepness employed. Initially, for both internal wave steepnesses, the slowly varying surface wave envelope is developed as the linear modulation theory predicts. As the steepness
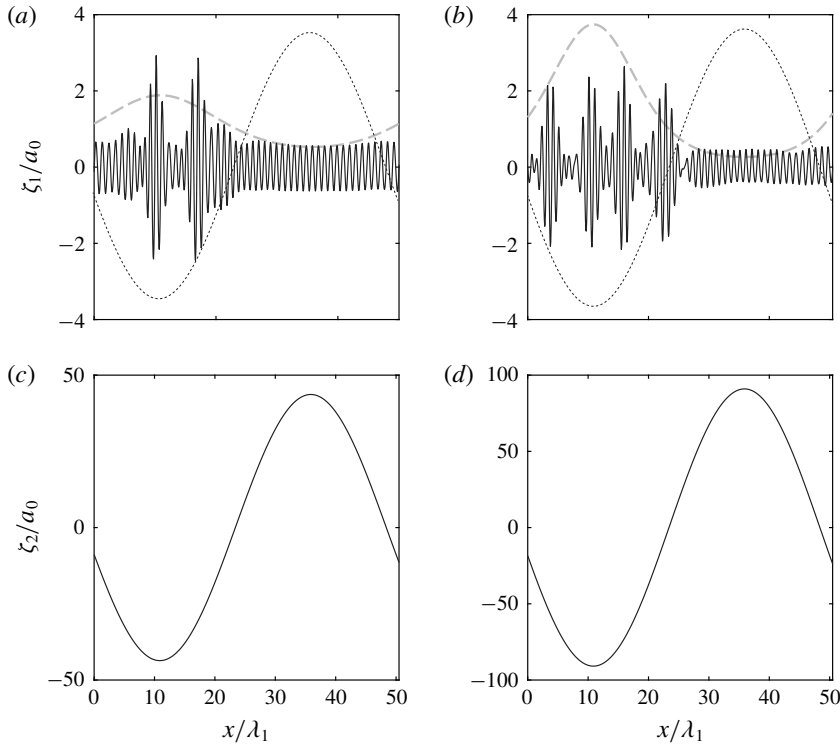
FIGURE 14. Surface and interface displacements at $\Omega t = 80$ over one internal wavelength from the numerical solutions shown in figure 13. (*a,b*) Surface wave displacements. (*c,d*) Internal wave displacements. (*a,c*) $\epsilon_I = 0.05$. (*b,d*) $\epsilon_I = 0.10$. Solid curves: simulated wave displacements. Dashed curves: theoretical upper wave envelope from (5.16) in § 5.2. Dotted curves: the interface displacements shown in (*b*) to display the relative phase between the surface and interface displacements. The displacements are normalized with the initial surface wave amplitude $a_0 = a_1(t = 0)$.

of the internal wave increases, the induced surface current grows. Then the surface waves deviate quickly from the prediction of the linear modulation theory and evolve into a number of groups.

An interesting feature observed from figure 13 is that a relatively broad single wave packet is initially formed as the linear modulation theory predicts, but then becomes localized as time increases. This process seems to repeat, but, after each cycle, the number of localized wave groups increases by one. This is related to the time-periodic exchange of wave energies through primary and subsequent resonant triad interactions, to be discussed later in this section.

Once again, as shown in figure 14, steep surface waves are observed right above where the internal wave troughs are located, which is consistent with the previous observation from figure 6 and the prediction of the linear modulation theory. While it fails to describe the detailed evolution and disintegration of wave groups, the linear modulation theory predicts reasonably well the location of highly modulated surface region.

Figure 15 shows a^* and m^* as functions of Ωt for surface wave steepness $\epsilon_S = 0.06$ and different internal wave steepnesses $\epsilon_I = 0.01$, 0.05 and 0.1. Both a^* and m^*
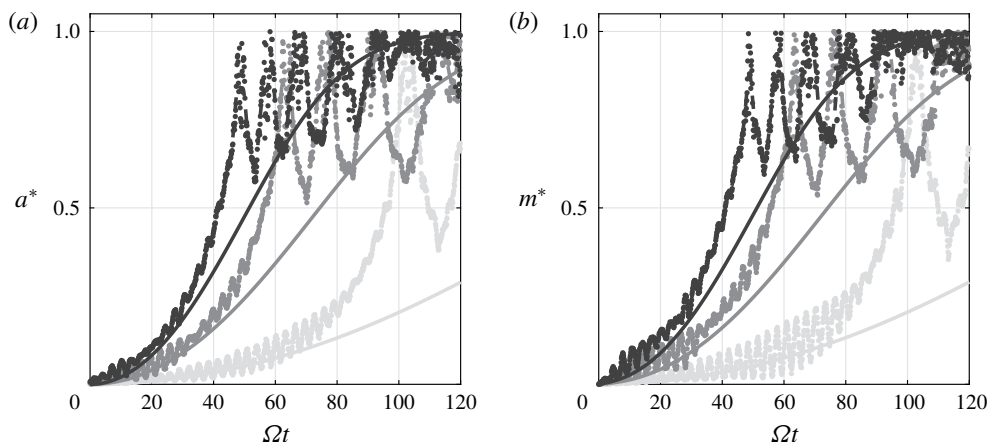
FIGURE 15. Amplitude and slope modulation, a^* and m^*, as functions Ωt for surface wave steepness $\epsilon_S = 0.06$ and three different internal wave steepnesses with oceanic parameters $\rho_1/\rho_2 = 0.99$ and $h_1/h_2 = 1/2$. Light grey: internal wave steepness $\epsilon_I = 0.01$. Dark grey: $\epsilon_I = 0.05$. Black: $\epsilon_I = 0.10$. Dots: simulation. Solid curves: linear modulation theory given by (5.19)–(5.20). Dashed curves: smoothed numerical solutions.

increases with the internal wave steepness. Initially, the numerical data are distributed close to the theoretical curves. As time increases, the numerical solutions under the realistic density condition show a qualitatively different behaviour compared to that observed from figure 10. After the initial exponential growth, the theory underestimates the modulation when it is compared with the numerical data and both a^* and m^* increase significantly faster. When the wave field is fully modulated, the wave fields display short recurrence periods and a^* and m^* reach the maximum theoretical value of one.

Figure 16 shows the time evolution of the surface wave amplitudes for a_1 and $a_{n\pm}$ ($n = 2, 3, \ldots, 11$) at k_1 and $k_{n\pm} = k_1 \pm (n-1)K$ for the simulation with $\epsilon_S = 0.06$ and $\epsilon_I = 0.1$. It is observed that, at $\Omega t = 20$, only $a_{n\pm}$ for $n = 2, 3, 4$ are exited significantly while all modes $a_{n\pm}$ are excited approximately equally at $\Omega t = 60$. Figure 16 shows that the initially monochromatic surface wave field evolves into a relatively broad-band spectrum of discrete modes $k_{n\pm}$ due to successive near-resonant interactions between long internal and short surface waves. The time evolution of the first few modes is shown in figure 17. Unlike the results shown in figure 11 for the parameters relevant for the experiment of Lewis *et al.* (1974), significant energy exchanges between primary and secondary triad modes are observed during their interactions. From (2.5), one can see that the group resonance condition becomes so close to the exact resonance condition as $K/k_1 \ll 1$ for the oceanic condition. Therefore, it can be concluded that the energy spread to the sidebands of the surface wave occurs more quickly as the density ratio is close to one.

8. Conclusion

We have developed a second-order Hamiltonian system describing the evolution of coupled surface and internal gravity waves and have investigated the evolution of short surface gravity waves interacting with a long internal wave under the group resonance condition. The Hamiltonian system conserving exactly the total energy is
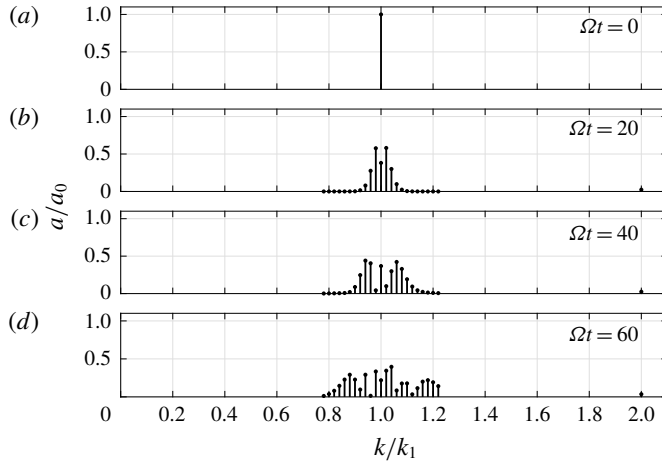
FIGURE 16. Snapshots of amplitude spectrum for a_1 and $a_{n\pm}$ ($n = 2, 3, \ldots, 11$) at k_1 and $k_{n\pm} = k_1 \pm (n-1)K$: (*a*) $\Omega t = 0$; (*b*) $\Omega t = 20$; (*c*) $\Omega t = 40$; (*d*) $\Omega t = 60$. Notice that all resonant waves appear near k_1 as $K/k_1 = 1/50$. The initial surface and internal wave steepnesses are given by $\epsilon_S = 0.06$ $\epsilon_I = 0.1$, respectively.
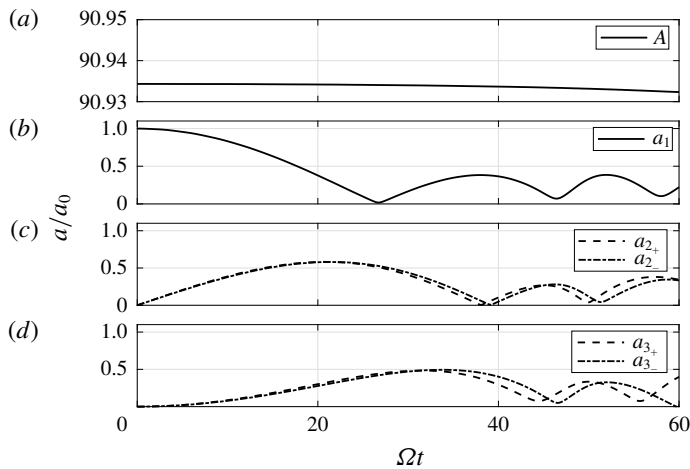

FIGURE 17. Time evolution of the amplitudes of surface and internal waves for the oceanic condition. (*a*) Internal wave amplitude A. (*b*) Surface wave amplitude a_1. (*c,d*): Near-resonant surface wave amplitudes a_{n+} (dashed curves) and a_{n-} (dash–dotted curves) for $n = 2, 3$. The amplitudes are normalized by the initial amplitude $a_0 = a_1(t = 0)$. The initial surface and internal wave steepnesses are given by $\epsilon_S = 0.06$ and $\epsilon_I = 0.1$, respectively.

written explicitly for four conjugate variables and describes the coupled motions of surface and internal waves of arbitrary wavelengths propagating in two horizontal dimensions. Special attention has been paid to surface wave modulation observed experimentally in a two-layer system by Lewis *et al.* (1974). We have attempted to reproduce the experimental observations of Lewis *et al.* (1974) on the envelope amplitude and slope variations.

When an internal wave with a relatively large amplitude is interacting with small amplitude surface waves, it is commonly assumed that the internal wave remains almost unchanged during their interactions and can be modelled as a known surface current. Then, the interaction between the surface and internal waves is formulated as a wave–current interaction problem, which is in turn studied using the linear modulation theory. In comparison of our numerical solutions with laboratory measurements and asymptotic solutions, it has been shown that this approach can be justified for the short-term evolution.

However, from our numerical simulations over a longer interaction period, it has been found that the linear modulation theory becomes invalid after the amplitudes of sidebands grow sufficiently. Then, it has been shown that the wave components satisfying approximately the condition for resonant triad interactions of class III start to exchange their energies. Of great interest is whether this physical process can be observed experimentally in a two-layer system, although such an experiment might be non-trivial.

Under a realistic oceanic condition, it has been observed that the bandwidth of surface waves quickly increases via successive near-resonant interactions and the evolution of such broadband waves cannot be easily described by a finite number of discrete modes governed by a low-dimensional dynamical system. In the present study, we have demonstrated that the second-order Hamiltonian system written explicitly in terms of conjugate variables in both physical and spectral spaces is a useful theoretical tool to study the resonant and near-resonant interactions of surface and internal waves of arbitrary bandwidths.

For physical parameters relevant for the oceanic condition, the wavelengths resolved in the simulations are much longer than those relevant for capillary waves and therefore the surface tension effect on the free surface has been neglected, although it can be easily included in the Hamiltonian system (Choi *et al.* 2020). For an interaction that occurs over a much longer time scale than $O(1/\epsilon)$ with ϵ being the wave steepness, a higher-order nonlinear simulation with the surface tension would be necessary.

Acknowledgements

Declaration of interests

The authors report no conflict of interest.

Appendix A. Various limits of the Hamiltonian system

A.1. *Linear system*

Under the small amplitude assumption, the system given by (3.38) can be linearized (Craig, Guyenne & Kalisch 2005) to

$$\frac{\partial \zeta_1}{\partial t} = \gamma_{11}\Psi_1 + \gamma_{12}\Psi_2, \quad \frac{\partial \zeta_2}{\partial t} = \gamma_{21}\Psi_1 + \gamma_{22}\Psi_2, \quad \frac{\partial \Psi_1}{\partial t} = -\rho_1 g\zeta_1, \quad \frac{\partial \Psi_2}{\partial t} = -\Delta\rho g\zeta_2.$$

$$(A\,1a{-}d)$$

When the linear solutions given by $(\zeta_1, \zeta_2, \Psi_1, \Psi_2) = (a_1, a_2, b_1, b_2) \exp[-i(kx - \omega t)]$ are substituted into (A 1), the equation for ω can be obtained as

$$\omega^4 - g(\rho_1\gamma_{11} + \Delta\rho\gamma_{22})\omega^2 + \rho_1\Delta\rho g^2(\gamma_{11}\gamma_{22} - \gamma_{12}\gamma_{21}) = 0, \tag{A 2}$$

which is equivalent to (2.1). The solutions of (A 2) yield the dispersion relations given by

$$\omega_{\pm}^2 = \frac{\rho_2 gk}{2(\rho_1 T_1 T_2 + \rho_2)}[(T_1 + T_2) \pm \sqrt{(T_1 + T_2)^2 - 4\Delta\rho(\rho_1 T_1 T_2 + \rho_2)T_1 T_2/\rho_2^2}]. \tag{A 3}$$

Notice that both ω_+ and ω_- are always real and represent the wave frequencies for the barotropic (surface wave) and baroclinic (internal wave) modes, respectively.

The amplitude ratio between the surface and interface displacements is given by

$$\frac{a_1}{a_2} = \left(\frac{\Delta\rho}{\rho_1}\right)\frac{b_1}{b_2} = \frac{\Delta\rho gkST_2}{\omega^2(\rho_1 T_1 T_2 + \rho_2) - gk(\rho_2 T_1 + \rho_1 T_2)} = \frac{S\omega^2}{\omega^2 - gkT_1}, \tag{A 4}$$

where (A 2) has been used for the last expression. It can be shown that the ratio is always positive for the barotropic mode ($\omega = \omega_+$) and negative for the baroclinic mode ($\omega = \omega_-$).

If the lower layer is infinitely deep ($h_2 \to \infty$) so that $T_2 = \tanh kh_2 \to 1$, equation (A 3) yields the dispersion relations (Lamb 1932) for the barotropic and baroclinic modes

$$\omega_+^2 = gk, \quad \omega_-^2 = \frac{\Delta\rho gkT_1}{\rho_1 T_1 + \rho_2}, \tag{A 5a,b}$$

respectively.

Under the Boussinesq approximation for small density jump, i.e. $\Delta\rho \ll \rho_2$, the solutions given by (A 3) can be approximated (Lamb 1932) by

$$\omega_+^2 = gkT_{1+2}\left[1 + O\left(\frac{\Delta\rho}{\rho_2}\right)\right], \quad \omega_-^2 = \frac{\Delta\rho gkT_1 T_2}{\rho_2(T_1 + T_2)}\left[1 + O\left(\frac{\Delta\rho}{\rho_2}\right)\right], \tag{A 6a,b}$$

where $T_{1+2} = \tanh[k(h_1 + h_2)]$. These correspond to the wave frequencies for surface waves in water of depth $h_1 + h_2$ and for internal waves in a two-layer system with a rigid top, respectively. The amplitude ratio can be then approximated as

$$\left(\frac{a_1}{a_2}\right)_+ \simeq \frac{T_1 + T_2}{ST_2} > 0, \quad \left(\frac{a_1}{a_2}\right)_- \simeq -\left(\frac{\Delta\rho}{\rho_2}\right)\frac{ST_2}{T_1 + T_2} < 0. \tag{A 7a,b}$$

To initialize the model, it is more convenient, for the surface wave mode, that b_1, b_2 and a_2 are expressed, in terms of the surface wave amplitude a_1, as

$$b_1 = \alpha_1 a_1, \quad b_2 = \alpha_2 a_1, \quad a_2 = \alpha_3 a_1, \tag{A 8a–c}$$

where

$$\alpha_1 = \frac{i\rho_1 g}{\omega}, \quad \alpha_2 = \frac{(i\omega - \gamma_{11}\alpha_1)}{\gamma_{12}}, \quad \alpha_3 = -\frac{i(\gamma_{21}\alpha_1 + \gamma_{22}\alpha_2)}{\omega}, \tag{A 9a–c}$$

while, for the internal wave mode, b_1, b_2 and a_1 are expressed, in terms of the internal wave amplitude a_2, as

$$b_1 = \beta_1 a_2, \quad b_2 = \beta_2 a_2, \quad a_1 = \beta_3 a_2, \tag{A 10a–c}$$

where

$$\beta_1 = \frac{(i\omega - \gamma_{22}\beta_2)}{\gamma_{21}}, \quad \beta_2 = \frac{i\Delta\rho g}{\omega}, \quad \beta_3 = -\frac{i(\gamma_{11}\beta_1 + \gamma_{12}\beta_2)}{\omega}. \tag{A 11a–c}$$

A.2. *Single layer*

For the case of a single layer of finite thickness h_2, substituting $\rho_1 = 0$ into (3.38c)–(3.38d) yields the second-order coupled equations for ζ_2 and $\Phi_2 = \Psi_2/\rho_2$

$$\frac{\partial \zeta_2}{\partial t} = kT_2\Phi_2 - kT_2(\zeta_2 kT_2\Phi_2) - \nabla \cdot (\zeta_2\nabla\Phi_2), \tag{A 12}$$

$$\frac{\partial \Phi_2}{\partial t} = -g\zeta_2 + \frac{1}{2}(kT_2\Phi_2)^2 - \frac{1}{2}(\nabla\Phi_2) \cdot (\nabla\Phi_2), \tag{A 13}$$

whose Hamiltonians are given, from (3.42)–(3.43), by

$$E_2 = \frac{\rho_2}{2}\int \left(g\zeta_2{}^2 + \Phi_2 kT_2\Phi_2\right)\mathrm{d}\boldsymbol{x}, \quad E_3 = -\frac{\rho_2}{2}\int \zeta_2[(kT_2\Phi_2)^2 - \nabla\Phi_2 \cdot \nabla\Phi_2]\mathrm{d}\boldsymbol{x}. \tag{A 14a,b}$$

Equations (A 12)–(A 13) are the system of nonlinear evolution equations obtained by Choi (1995) for surface waves when the system is truncated at the second order. The linear dispersion relation for this system can be obtained as $\omega^2 = gkT_2$.

A.3. *Infinitely deep layers*

For the case of infinitely deep layers ($h_i \to \infty$ for i=1, 2), from

$$T_i = \tanh kh_i \to 1, \quad S = \mathrm{sech}\,kh_1 \to 0, \quad J = 1/(\rho_1 T_1 T_2 + \rho_2) \to 1/(\rho_1 + \rho_2), \tag{A 15a-c}$$

the system for the upper layer given by (3.38a)–(3.38b) can be reduced to

$$\frac{\partial \zeta_1}{\partial t} = k\Psi_1/\rho_1 - \nabla \cdot (\zeta_1\nabla\Psi_1)/\rho_1 - k(\zeta_1 k\Psi_1/\rho_1), \tag{A 16}$$

$$\frac{\partial \Psi_1}{\partial t} = -\rho_1 g\zeta_1 - \frac{1}{2}\left|\nabla\Psi_1\right|^2/\rho_1 + \frac{1}{2}(k\Psi_1)^2/\rho_1, \tag{A 17}$$

while the system for the lower layer given by (3.38c)–(3.38d) becomes

$$\frac{\partial \zeta_2}{\partial t} = \frac{1}{\rho_1 + \rho_2}\left[k\Psi_2 - \frac{\Delta\rho}{\rho_1 + \rho_2}k(\zeta_2 k\Psi_2) - \frac{\Delta\rho}{\rho_1 + \rho_2}\nabla \cdot (\zeta_2\nabla\Psi_2)\right], \tag{A 18}$$

$$\frac{\partial \Psi_2}{\partial t} = -\Delta\rho g\zeta_2 + \frac{1}{2}\frac{\Delta\rho}{(\rho_1 + \rho_2)^2}\left[(k\Psi_2)^2 - |\nabla\Psi_2|^2\right]. \tag{A 19}$$

As the top free surface is too far away from the interface, the system for the upper layer given by (A 16)–(A 17) is completely decoupled from that for the lower layer and can be transformed to that for the case of infinitely deep single layer given by (A 12)–(A 13) with $T_2 \to 1$ by making the transformations given by $\widehat{\zeta_2} = \zeta_1$ and $\widehat{\Phi_2} = \Psi_1/\rho_1$.

On the other hand, the system for the lower layer given by (A 18)–(A 19) describes the internal wave motion between two infinitely deep fluids, whose linear dispersion relation is given by

$$\omega^2 = \frac{\Delta\rho}{\rho_1 + \rho_2}gk. \tag{A 20}$$

One interesting observation is that (A 18)–(A 19) can be also transformed to (A 12)–(A 13) or (A 16)–(A 17) by making simple transformations. For example,

one can recover (A 16)–(A 17) from (A 18)–(A 19) by introducing the following new variables

$$\widehat{\Psi}_1 = \frac{\rho_1}{\rho_1 + \rho_2}\left(\frac{\Delta\rho}{\rho_1 + \rho_2}\right)^{1/2}\Psi_2, \quad \widehat{\zeta}_1 = \left(\frac{\Delta\rho}{\rho_1 + \rho_2}\right)\zeta_2, \quad \widehat{t} = \left(\frac{\Delta\rho}{\rho_1 + \rho_2}\right)^{1/2}t.$$

$$(A\,21a-c)$$

Appendix B. Linear modulation theory: asymptotic solutions

From (5.12)–(5.14), the governing equations for k, a^2 and x can be written (Lewis *et al.* 1974) as

$$\frac{\mathrm{d}\ln k}{\mathrm{d}\tau} = -\frac{\partial U}{\partial x}, \quad \frac{\mathrm{d}\ln a^2}{\mathrm{d}\tau} = -\frac{3}{2}\frac{\partial U}{\partial x} - \frac{\partial c_g}{\partial x}, \quad \frac{\mathrm{d}x}{\mathrm{d}\tau} = c_g + U. \qquad (\mathrm{B}\,1a-c)$$

By assuming $\varepsilon = U_0/C \ll 1$, the solutions $f = (\ln k, \ln a^2, x)$ can be expanded in ε as

$$f = \varepsilon^0 f_0 + \varepsilon^1 f_1 + \varepsilon^2 f_2 + \cdots, \qquad (\mathrm{B}\,2)$$

where $f_j = O(1)$ for $j = 1, 2, \cdots$. In addition, from (B 2) for $\ln k$, the group velocity of the surface wave $c_g(k)$ can be expanded as

$$c_g = \varepsilon^0 c_{g0} + \varepsilon^1 c_{g1} + \varepsilon^2 c_{g2} + \cdots, \qquad (\mathrm{B}\,3)$$

where $c_{g0} = c_g(k_0)$ and $c_{g1} = -\frac{1}{2}c_{g0}\ln k_1$.

Substituting (B 2)–(B 3) into (B 1), one obtains at $O(\varepsilon^0)$

$$\frac{\mathrm{d}k_0}{\mathrm{d}\tau} = 0, \quad \frac{\mathrm{d}a_0^2}{\mathrm{d}\tau} = 0, \quad \frac{\mathrm{d}x_0}{\mathrm{d}\tau} = c_{g0}, \qquad (\mathrm{B}\,4a-c)$$

whose solutions represent the unperturbed monochromatic surface wave in the absence of the surface current $U(x)$. Integration of (B 4) gives k_0=constant, a_0=constant and

$$x_0 = c_{g0}\tau + \xi, \qquad (\mathrm{B}\,5)$$

from the initial condition given by $x_0 = \xi$ at $\tau = 0$.

At $O(\varepsilon)$, employing (5.3) for $U(x)$, the governing equations for k_1 and a_1^2 can be found as

$$\frac{\mathrm{d}\ln k_1}{\mathrm{d}\tau} = -U_0 K \sin K(x_0 - C\tau), \qquad (\mathrm{B}\,6)$$

$$\frac{\mathrm{d}\ln a_1^2}{\mathrm{d}\tau} = -\frac{3}{2}U_0 K \sin K(x_0 - C\tau) - \frac{\partial c_{g1}}{\partial x}, \qquad (\mathrm{B}\,7)$$

which represent the first-order change of the wavenumber and the square of the amplitude of the surface wave envelope. Using the zeroth-order solution for x_0 given by (B 5),

$$x_0 - C\tau = (c_{g0} - C)\tau + \xi, \qquad (\mathrm{B}\,8)$$

equations (B 6)–(B 7) can be integrated with respect to τ from zero to t along the characteristic ξ with $\ln k_1 = \ln a_1 = 0$ at $\tau = 0$. Then, the solutions are obtained as

$$\ln k_1 = \frac{U_0}{c_{g0} - C}(\cos\theta_1 - \cos\theta_2), \qquad (\mathrm{B}\,9)$$

$$\ln a_1 = \frac{1}{4} \frac{U_0}{c_{g0} - C} \left[\left(3 + \frac{c_{g0}}{c_{g0} - C} \right) (\cos \theta_1 - \cos \theta_2) + c_{g0} K t \sin \theta_2 \right]. \quad \text{(B 10)}$$

Here, θ_1 and θ_2 are defined as

$$\theta_1 = K(x - Ct), \quad \theta_2 = K(x - c_{g0}t), \quad \text{(B 11a,b)}$$

where x_0 has been replaced by x under the same order of approximation.

Then, from $\ln k_1 = \ln(k/k_0)$ and $\ln a_1 = \ln(a/a_0)$, equations (B 9)–(B 10) can be re-written as

$$k(x, t) = k_0 \exp \left[\frac{U_0}{c_{g0} - C} (\cos \theta_1 - \cos \theta_2) \right], \quad \text{(B 12)}$$

$$a(x, t) = a_0 \exp \left[\frac{1}{4} \frac{U_0}{c_{g0} - C} \left\{ \left(3 + \frac{c_{g0}}{c_{g0} - C} \right) (\cos \theta_1 - \cos \theta_2) + c_{g0} K t \sin \theta_2 \right\} \right]. \quad \text{(B 13)}$$

As $c_{g0} \to C$, after rewriting $\cos \theta_1 - \cos \theta_2$ using trigonometric identities and expanding to leading order, equations (B 9) and (B 10) can be reduced to the results given by (5.15)–(5.16).

Instead of (5.3), Lewis *et al.* (1974) used the current $U(x, t)$ given by

$$U(x, t) = U_0 \sin K(x - Ct) H(x) H(t - x/C), \quad \text{(B 14)}$$

where $H(x)$ is the Heaviside function representing the current field downstream from the wavemaker at $x = 0$. As the current field is generated by an internal wave of the phase speed C, it is observed only for $x < Ct$. In particular, in the limit of $c_{g0} \to C$, their solutions for a and k are given by

$$\ln \frac{k}{k_0} = -\frac{U_0}{C} H(x) H(t - x/C) \{ \sin K(x - Ct) + Kx \cos K(x - Ct) \}, \quad \text{(B 15)}$$

$$\ln \frac{a}{a_0} = -\frac{U_0}{4C} H(x) H(t - x/C) \left\{ \left(4 - \frac{1}{2} K^2 x^2 \right) \sin K(x - Ct) + 5Kx \cos K(x - Ct) \right\}. \quad \text{(B 16)}$$

Appendix C. Amplitude equations for class-III resonance

As shown in Choi *et al.* (2020), the Hamiltonian system (3.38) can be written in spectral space as

$$\frac{\partial \boldsymbol{a}}{\partial t} = \frac{\delta H}{\delta \boldsymbol{b}^*}, \quad \frac{\partial \boldsymbol{b}}{\partial t} = -\frac{\delta H}{\delta \boldsymbol{a}^*}, \quad \text{(C 1a,b)}$$

where $\boldsymbol{a} = (a_1, a_2)^{\mathrm{T}}$ and $\boldsymbol{b} = (b_1, b_2)^{\mathrm{T}}$ represent the Fourier transforms of $(\zeta_1, \zeta_2)^{\mathrm{T}}$ and $(\Psi_1, \Psi_2)^{\mathrm{T}}$, respectively. Then, the following canonical transformation is introduced to decompose the surface and interface motions into the barotropic and baroclinic components

$$\begin{pmatrix} \boldsymbol{a} \\ \boldsymbol{b} \end{pmatrix} = \begin{pmatrix} \boldsymbol{Q} & O \\ O & \boldsymbol{P} \end{pmatrix} \begin{pmatrix} \boldsymbol{q} \\ \boldsymbol{p} \end{pmatrix}, \quad \text{(C 2)}$$

where $\boldsymbol{p} = (p_+, p_-)^{\mathrm{T}}$ and $\boldsymbol{q} = (q_+, q_-)^{\mathrm{T}}$ with the subscripts $+$ and $-$ representing the barotropic and baroclinic modes. In (C 2), $\boldsymbol{Q}$ and $\boldsymbol{P}$ are 2×2 matrices given by

$$\boldsymbol{Q} = \boldsymbol{M} \boldsymbol{S}^{1/2} = \begin{pmatrix} Q^{(1,1)} & Q^{(1,2)} \\ Q^{(2,1)} & Q^{(2,2)} \end{pmatrix}, \quad \boldsymbol{P} = \Gamma^{-1} \boldsymbol{M} \boldsymbol{S}^{1/2} = \begin{pmatrix} P^{(1,1)} & P^{(1,2)} \\ P^{(2,1)} & P^{(2,2)} \end{pmatrix}, \quad \text{(C 3a,b)}$$

where $\boldsymbol{S} = \boldsymbol{M}^{-1}\boldsymbol{\varGamma}(\boldsymbol{M}^{-1})^{\mathrm{T}}$, and $\boldsymbol{\varGamma}$ and $\boldsymbol{M}$ are given by

$$\boldsymbol{\varGamma} = \begin{pmatrix} \gamma_{11} & \gamma_{12} \\ \gamma_{21} & \gamma_{22} \end{pmatrix}, \quad \boldsymbol{M} = \begin{pmatrix} (\omega_+^2 - \Delta\rho g\gamma_{22})n_+ & \Delta\rho g\gamma_{12}n_- \\ \rho_u g\gamma_{21}n_+ & (\omega_-^2 - \rho_u g\gamma_{11})n_- \end{pmatrix}, \quad \text{(C 4a,b)}$$

with n_+ and n_- given by

$$n_+ = [(\omega_+^2 - \Delta\rho\gamma_{22})^2 + (\rho_u g\gamma_{21})^2]^{-1/2}, \quad n_- = [(\rho_u g\gamma_{21})^2 + (\omega_-^2 - \rho_u g\gamma_{11})^2]^{-1/2}. \quad \text{(C 5a,b)}$$

Then, by introducing the complex amplitude functions defined by

$$\mathcal{A}(\boldsymbol{k}, t) = \sqrt{\frac{\omega_+}{2}}\left(q_+ - \mathrm{i}\frac{p_+}{\omega_+}\right)\mathrm{e}^{-\mathrm{i}\omega_+ t}, \quad \mathcal{B}(\boldsymbol{k}, t) = \sqrt{\frac{\omega_-}{2}}\left(q_- - \mathrm{i}\frac{p_-}{\omega_-}\right)\mathrm{e}^{-\mathrm{i}\omega_- t}, \quad \text{(C 6a,b)}$$

the slowly varying amplitude equations relevant for the class-III resonance condition can be obtained (Choi *et al.* 2020) as

$$\frac{\mathrm{d}\mathcal{A}_1}{\mathrm{d}t} = \mathrm{i}V_{1,2,3}^{(2)}\mathcal{A}_2\mathcal{B}_3, \quad \frac{\mathrm{d}\mathcal{A}_2}{\mathrm{d}t} = \mathrm{i}V_{1,2,3}^{(2)}\mathcal{A}_1\mathcal{B}_3^*, \quad \frac{\mathrm{d}\mathcal{B}_3}{\mathrm{d}t} = \mathrm{i}V_{1,2,3}^{(2)}\mathcal{A}_1\mathcal{A}_2^*, \quad \text{(C 7a–c)}$$

where $\mathcal{A}_j = \mathcal{A}(\boldsymbol{k}_j)$ ($j = 1, 2$) and $\mathcal{B}_3 = \mathcal{B}(\boldsymbol{k}_3)$ represent the amplitudes of the barotropic and baroclinic modes, respectively. The coefficient of the amplitude equations is given by

$$V_{1,2,3}^{(2)} = -\overline{U}_{-1,3,2}^{(2)} + \overline{U}_{2,3,-1}^{(2)} - \overline{U}_{-1,2,3}^{(4)} - \overline{U}_{2,-1,3}^{(4)}, \quad \text{(C 8)}$$

where

$$\overline{U}_{1,2,3}^{(2)} = -\sqrt{\frac{\omega_1^+\omega_2^-}{8\omega_3^+}}U_{1,2,3}^{(2)}, \quad \overline{U}_{1,2,3}^{(4)} = -\sqrt{\frac{\omega_1^+\omega_2^+}{8\omega_3^-}}U_{1,2,3}^{(4)}, \quad \text{(C 9a,b)}$$

$$\begin{aligned} U_{1,2,3}^{(2)} = {} & 2h_{1,2,3}^{(1)}P_1^{(1,1)}P_2^{(1,2)}Q_3^{(1,1)} + h_{1,2,3}^{(2)}P_1^{(1,1)}P_2^{(2,2)}Q_3^{(1,1)} + h_{2,1,3}^{(2)}P_1^{(2,1)}P_2^{(1,2)}Q_3^{(1,1)} \\ & + 2h_{1,2,3}^{(3)}P_1^{(2,1)}P_2^{(2,2)}Q_3^{(1,1)} + 2h_{1,2,3}^{(4)}P_1^{(1,1)}P_2^{(1,2)}Q_3^{(2,1)} \\ & + h_{1,2,3}^{(5)}P_1^{(1,1)}P_2^{(2,2)}Q_3^{(2,1)} + h_{2,1,3}^{(5)}P_1^{(2,1)}P_2^{(1,2)}Q_3^{(2,1)} + 2h_{1,2,3}^{(6)}P_1^{(2,1)}P_2^{(2,2)}Q_3^{(2,1)}, \end{aligned}$$

$$\text{(C 10)}$$

$$\begin{aligned} U_{1,2,3}^{(4)} = {} & h_{1,2,3}^{(1)}P_1^{(1,1)}P_2^{(1,1)}Q_3^{(1,2)} + h_{1,2,3}^{(2)}P_1^{(1,1)}P_2^{(2,1)}Q_3^{(1,2)} + h_{1,2,3}^{(3)}P_1^{(2,1)}P_2^{(2,1)}Q_3^{(1,2)} \\ & + h_{1,2,3}^{(4)}P_1^{(1,1)}P_2^{(1,1)}Q_3^{(2,2)} + h_{1,2,3}^{(5)}P_1^{(1,1)}P_2^{(2,1)}Q_3^{(2,2)} + h_{1,2,3}^{(6)}P_1^{(2,1)}P_2^{(2,1)}Q_3^{(2,2)}, \end{aligned}$$

$$\text{(C 11)}$$

with

$$h_{1,2,3}^{(1)} = -\tfrac{1}{2}(\boldsymbol{k}_1 \cdot \boldsymbol{k}_2)/\rho_1 - \tfrac{1}{2}\rho_u\gamma_{11,1}\gamma_{11,2}, \quad \text{(C 12)}$$

$$h_{1,2,3}^{(2)} = -\rho_u\gamma_{11,1}\gamma_{12,2}, \quad h_{1,2,3}^{(3)} = -\tfrac{1}{2}\rho_u\gamma_{12,1}\gamma_{12,2}, \quad \text{(C 13)}$$

$$h_{1,2,3}^{(4)} = -\tfrac{1}{2}\Delta\rho[-(\rho_l/\rho_u)\gamma_{31,1}\gamma_{31,2}(\boldsymbol{k}_1 \cdot \boldsymbol{k}_2) + \gamma_{21,1}\gamma_{21,2}], \quad \text{(C 14)}$$

$$h_{1,2,3}^{(5)} = -\Delta\rho\gamma_{21,1}\gamma_{22,2} - \rho_l\gamma_{31,1}\gamma_{33,2}(\boldsymbol{k}_1 \cdot \boldsymbol{k}_2), \quad \text{(C 15)}$$

$$h_{1,2,3}^{(6)} = -\tfrac{1}{2}[\Delta\rho\gamma_{22,1}\gamma_{22,2} + (\rho_l\gamma_{30,1}\gamma_{30,2} - \rho_u\gamma_{32,1}\gamma_{32,2})(\boldsymbol{k}_1 \cdot \boldsymbol{k}_2)]. \quad \text{(C 16)}$$

Notice that $\omega_j^\pm = \omega_\pm(\boldsymbol{k}_j)$, $\gamma_{lm,j} = \gamma_{lm}(\boldsymbol{k}_j)$, $P_j^{(l,m)} = P^{(l,m)}(\boldsymbol{k}_j)$ and $Q_j^{(l,m)} = Q^{(l,m)}(\boldsymbol{k}_j)$.

REFERENCES

ALAM, M.-R. 2012 A new triad resonance between co-propagating surface and interfacial waves. *J. Fluid Mech.* **691**, 267–278.

ALAM, M.-R., LIU, Y. & YUE, D. K. P. 2009 Bragg resonance of waves in a two-layer fluid propagating over bottom ripples. Part II. Numerical simulation. *J. Fluid Mech.* **624**, 225–253.

ALPERS, W. 1985 Theory of radar imaging of internal waves. *Nature* **314**, 245–247.

BALL, F. K. 1964 Energy transfer between external and internal gravity waves. *J. Fluid Mech.* **19**, 465–478.

BENJAMIN, T. B. & BRIDGES, T. J. 1997 Reappraisal of the Kelvin-Helmholtz problem. Part 1. Hamiltonian structure. *J. Fluid Mech.* **333**, 301–325.

BENNEY, D. J. 1977 A general theory for interactions between short and long waves. *Stud. Appl. Maths* **56**, 81–94.

BRETHERTON, F. P. & GARRETT, C. J. R. 1969 Wavetrains in inhomogeneous moving media. *Proc. R. Soc. Lond.* A **302**, 529–554.

CHOI, W. 1995 Nonlinear evolution equations for two-dimensional surface waves in a fluid of finite depth. *J. Fluid Mech.* **295**, 381–394.

CHOI, W., CHABANE, M. & TAKLO, T. M. A. 2020 Two-dimensional resonant triad interactions in a two-layer system. *J. Fluid Mech.* (submitted).

CHOI, W. & LYZENGA, D. R. 2006 Nonlinear surface wave dynamics in slowly varying ocean environments. In *Proceedings of the 26th Symposium on Naval Hydrodynamics, Rome, Italy*, pp. 1–9.

CRAIG, W., GUYENNE, P. & KALISCH, H. 2005 Hamiltonian long-wave expansions for free surfaces and interfaces. *Commun. Pure Appl. Maths* **58**, 1587–1641.

CRAIG, W., GUYENNE, P. & SULEM, C. 2012 The surface signature of internal waves. *J. Fluid Mech.* **710**, 277–303.

EWING, G. 1950 Slicks, surface films and internal waves. *J. Mar. Res.* **9**, 161–187.

FUNAKOSHI, M. & OIKAWA, M. 1983 The resonant interaction between a long internal gravity wave and a surface gravity wave packet. *J. Phys. Soc. Japan* **52**, 1982–1995.

GARGETT, A. E. & HUGHES, B. A. 1972 On the interaction of surface and internal waves. *J. Fluid Mech.* **52**, 179–191.

GASPAROVIC, R. F., APEL, J. R. & KASISCHKE, E. S. 1988 An overview of the SAR internal wave experiment. *J. Geophys. Res.* **93**, 12304–12315.

HILL, D. F. & FODA, M. A. 1996 Subharmonic resonance of short internal standing waves by progressive surface waves. *J. Fluid Mech.* **321**, 217–233.

HUGHES, B. A. 1978 The effect of internal waves on surface wind waves 2. Theoretical analysis. *J. Geophys. Res.* **83**, 455–465.

HUGHES, B. A. & GRANT, H. L. 1978 The effect of internal waves on surface wind waves 1. Experimental measurements. *J. Geophys. Res.* **83**, 443–454.

HWUNG, H.-H., YANG, R.-Y. & SHUGAN, I. V. 2009 Exposure of internal waves on the sea surface. *J. Fluid Mech.* **626**, 1–20.

JIANG, S. W., KOVACIC, G., ZHOU, D. & CAI, D. 2019 Modulation-resonance mechanism for surface waves in a two-layer fluid system. *J. Fluid Mech.* **875**, 807–841.

JO, T.-C. & CHOI, W. 2008 On stabilizing the strongly nonlinear internal wave model. *Stud. Appl. Maths* **120**, 65–85.

KAWAHARA, T., SUGIMOTO, N. & KAKUTANI, T. 1975 Nonlinear interaction between short and long capillary-gravity waves. *J. Phys. Soc. Japan* **39**, 1379–1386.

KODAIRA, T., WASEDA, T., MIYATA, M. & CHOI, W. 2016 Internal solitary waves in a two-fluid system with a free surface. *J. Fluid Mech.* **804**, 201–223.

LAFOND, E. C. 1962 Internal waves, Part I in N. M. Hill, The Sea. *Interscience* **1**, 731–751.

LAMB, H. 1932 *Hydrodynamics*, 6th edn. Dover.

LEWIS, J. E., LAKE, B. M. & KO, D. R. S. 1974 On the interaction of internal waves and surface gravity waves. *J. Fluid Mech.* **63**, 773–800.

LONGUET-HIGGINS, M. S. & STEWART, R. W. 1960 Changes in the form of short gravity waves on long waves and tidal currents. *J. Fluid Mech.* **8**, 565–583.

LONGUET-HIGGINS, M. S. & STEWART, R. W. 1961 The change in amplitude of short gravity waves on steady non-uniform currents. *J. Fluid Mech.* **10**, 529–549.

MCGOLDRICK, L. F. 1965 Resonant interactions among capillary-gravity waves. *J. Fluid Mech.* **21**, 305–331.

OSBORNE, A. R. & BURCH, T. L. 1980 Internal solitons in the Andaman sea. *Science* **208**, 451–460.

PHILLIPS, O. M. 1960 On the dynamics of unsteady gravity waves of finite amplitude. Part 1. The elementary interactions. *J. Fluid Mech.* **9**, 193–217.

PHILLIPS, O. M. 1977 *Dynamics of the Upper Ocean Layer*. John Wiley & Sons.

SEGUR, H. 1980 Resonant interactions of surface and internal gravity waves. *Phys. Fluids Res. Notes* **23**, 2556–2557.

TANAKA, M. & WAKAYAMA, K. 2015 A numerical study on the energy transfer from surface waves to interfacial waves in a two-layer fluid system. *J. Fluid Mech.* **763**, 202–217.

THORPE, S. A. 1968 On the shape of progressive internal waves. *Phil. Trans. R. Soc. Lond.* A **263**, 563–614.

WATSON, G. & ROBINSON, I. S. 1990 A study of internal wave propagation in the strait of Gibraltar using shore-based marine radar images. *J. Phys. Oceanogr.* **20**, 374–395.

WEN, F. 1995 Resonant generation of internal waves on the soft sea bed by a surface water wave. *Phys. Fluids* **7**, 1915–1922.

WHITHAM, G. B. 1962 Mass, momentum and energy flux in water waves. *J. Fluid Mech.* **12**, 135–147.